



HAL
open science

On the Dynamics of the Southern Senegal Upwelling Center: Observed Variability from Synoptic to Superinertial Scales

Xavier Capet, Philippe Estrade, Éric Machu, Siny Ndoye, Jacques Grelet, Alban Lazar, Louis Marié, Denis Dausse, Patrice Brehmer

► **To cite this version:**

Xavier Capet, Philippe Estrade, Éric Machu, Siny Ndoye, Jacques Grelet, et al.. On the Dynamics of the Southern Senegal Upwelling Center: Observed Variability from Synoptic to Superinertial Scales. *Journal of Physical Oceanography*, 2017, 47 (1), pp.155 - 180. 10.1175/JPO-D-15-0247.1 . hal-01450642

HAL Id: hal-01450642

<https://hal.science/hal-01450642>

Submitted on 6 Feb 2017

HAL is a multi-disciplinary open access archive for the deposit and dissemination of scientific research documents, whether they are published or not. The documents may come from teaching and research institutions in France or abroad, or from public or private research centers.

L'archive ouverte pluridisciplinaire **HAL**, est destinée au dépôt et à la diffusion de documents scientifiques de niveau recherche, publiés ou non, émanant des établissements d'enseignement et de recherche français ou étrangers, des laboratoires publics ou privés.

18

Louis Marié

19

Laboratoire de Physique des Océans, Plouzané, France

20

Denis Dausse

21

LOCEAN Laboratory, CNRS-IRD-Sorbonne Universités, UPMC, MNHN, Paris, France

22

Patrice Brehmer

23

Institut Sénégalais de Recherche Agronomique, Centre de Recherche Oc Océographique

24

Dakar-Thiaroye, Dakar, Senegal

25 **Corresponding author address: LOCEAN, 4 place Jussieu, 75005 Paris, France.*

26 E-mail: xclod@locean-ipsl.upmc.fr

ABSTRACT

27 Upwelling off southern Senegal and Gambia takes place over a wide shelf
28 with a large area where depths are shallower than 20 m. This results in typical
29 upwelling patterns that are distinct (*e.g.*, more persistent in time and aligned
30 alongshore) from those of other better known systems, including Oregon and
31 Peru where inner shelves are comparatively narrow. Synoptic to superinertial
32 variability of this upwelling center is captured through a four week intensive
33 field campaign, representing the most comprehensive measurements of this
34 region to-date. The influence of mesoscale activity extends across the shelf
35 break and far over the shelf where it impacts the mid-shelf upwelling (*e.g.*,
36 strength of the upwelling front and circulation), possibly in concert with wind
37 fluctuations. Internal tides and solitary waves of large amplitude are ubiqui-
38 tous over the shelf. Our observations suggest that these and possibly other
39 sources of mixing play a major role in the overall system dynamics through
40 their impact upon the general shelf thermohaline structure, in particular in the
41 vicinity of the upwelling zone. Systematic alongshore variability in thermo-
42 haline properties highlight important limitations of the 2D idealization frame-
43 work that is frequently used in coastal upwelling studies.

44 **1. Introduction**

45 Coastal upwelling systems have received widespread attention for several decades owing to their
46 importance for human society. Although the primary driving mechanism is generic, important
47 differences exist between systems and also between sectors of each given system. Stratification,
48 shelf/slope topographic shapes, coastline irregularities and subtleties in the wind spatial/temporal
49 structure have a major impact on upwelling water pathways and overall dynamical, hydrological,
50 biogeochemical (Messié and Chavez 2015) and ecological (Pitcher et al. 2010) characteristics of
51 upwelling regions. Over the past decade processes associated with short time scales (daily and
52 higher) have progressively been incorporated into our knowledge base, adding further complexity
53 as we account for local specifics.

54 These advances have to a large extent taken place in the California Current System (Woodson
55 et al. 2007, 2009; Ryan et al. 2010; Kudela et al. 2008; Lucas et al. 2011a) and to a lesser extent
56 in the Benguela system (Lucas et al. 2014). Conversely, our understanding of West African up-
57 wellings remains to a large extent superficial (*i.e.*, guided by satellite and sometimes surface in
58 situ measurements; Roy 1998; Demarcq and Faure 2000; Lathuilière et al. 2008), low-frequency
59 and relatively large scale. A notable exception is Schafstall et al. (2010) with an estimation of
60 diapycnal nutrient fluxes due to internal wave dissipation over the Mauritanian shelf.

61 The large scale dynamics and hydrology of the southern end of the Canary system has, on
62 the other hand, been known for a long time. Between the Cape Verde frontal zone (which runs
63 approximately between Cape Blanc ($\sim 21^{\circ}\text{N}$, Mauritania) and the Cape Verde archipelago (Barton
64 1998), see Fig. 1) and Cape Roxo ($12^{\circ} 20'\text{N}$) the wind regime is responsible for quasi-permanent
65 Ekman pumping and winter/spring coastal upwelling. The former extends hundreds of kilometers
66 offshore and drives a large scale cyclonic circulation whose manifestation includes the Mauritanian

67 Current (MC hereafter, see Fig. 1). The MC differs from poleward undercurrents typical of many
68 upwelling systems in that it is generally intensified at or close to the surface (Peña-Izquierdo et al.
69 2012; Barton 1989), reflecting the strength of the forcing. In the south, the MC connects with
70 the complex equatorial current system and the connection involves a quasi-stationary cyclonic
71 feature, the Guinea dome (more details can be found in Barton 1998, Aristegui et al. 2009). Fig. 1
72 is suggestive of the role of the MC in maintaining a relatively warm environment in the immediate
73 vicinity of the shelf break over the latitude band 12° - 17° N, despite sustained coastal upwelling.

74 Seasonality of hydrology and circulation of the coastal ocean off this part of West Africa are
75 tightly controlled by the displacements of the Inter-Tropical Convergence Zone (Citeau et al.
76 1989). During the monsoon season (Jul.- Oct.) weak westerly winds (interrupted by the pas-
77 sage of occasional storms and easterly waves) dominate and the region receives the overwhelming
78 fraction of its annual precipitation. From approximately November to May the ITCZ is located to
79 the south and upwelling favorable trade winds dominate. Their peak intensity is in February-April,
80 our period of interest, during which precipitation and river run-off is insignificant.

81 Two coastal sectors can be distinguished in this region, based on distinctions between their
82 atmospheric forcings, influence of the surrounding ocean, and shelf/slope morphology. North of
83 the Cape Verde peninsula the shelf is relatively narrow (up to the Banc d'Arguin at $\sim 20^{\circ}$ N) and,
84 because this is the northern limit of the ITCZ migration, the upwelling season here is longest.

85 This study reports and analyses observations carried out in the southern sector offshore of south-
86 ern Senegal (between the Cape Verde peninsula and $\sim 13^{\circ}40'$ N, see Fig. 1) during 2 consecutive
87 field experiments (amounting to 25 days at sea) carried out in February-March 2012-2013, *i.e.*,
88 the core of the upwelling season. The general strategy was to cover a relatively limited area of \sim
89 1° by 1° (Fig. 1) multiple times, taking measurements of physical, biogeochemical and ecological

90 parameters. We herein focus on the physics but the role of this coastal region as fishing ground
91 and small pelagic fish nursery is an important motivation for this work.

92 During the upwelling season the southern sector acts as an upwelling center referred to as South-
93 ern Senegal upwelling center (SSUC) below. The terminology "upwelling center" refers to the
94 existence of a well-identified and persistent focal point where upwelling is enhanced and from
95 which a cold tongue originates, as vividly revealed by SST images (Fig. 1). In upwelling sys-
96 tems with intense mesoscale turbulence cold upwelling tongues take the form of filaments which
97 are predominantly directed toward the slope and open ocean (Strub et al. 1991) and thus strongly
98 contribute to cross-shore exchanges. Mesoscale activity is not particularly intense in the Canary
99 system (Capet et al. 2008b; Marchesiello and Estrade 2009). In addition, the SSUC is mostly char-
100 acterised by a wide shelf. South of $14^{\circ}30'N$ the shelf break, roughly defined by the 100 m isobath,
101 is 50 km away from shore or more while water depth is less than 30 m over a 1/3 to 1/2 of the shelf
102 area (*e.g.*, see Fig. 3). Thus, coastal upwelling in the SSUC is partly sheltered from the mesoscale
103 influence taking place over the continental slope and open ocean. This has several related impli-
104 cations: the general orientation of the cold upwelling tongue is north to south and, judging from
105 SST images, it preserves its coherence over long distances (up to three-four hundred kilometers in
106 some circumstances, Ndoye et al. 2014)¹; temporal stability of the tongue is also noticeable over
107 periods of many days to weeks; export from the shelf to the open ocean is retarded.

108 This being said, the degree of insulation between shelf upwelling dynamics and offshore turbu-
109 lent activity needs to be qualified. South of $14^{\circ}30'N$, the upwelling tongue is frequently found 50
110 km or more away from the coast. Its offshore edge, generally referred to as the upwelling front, is

¹Note however that incorporation of subsurface water in the tongue tens to hundreds of kilometers from its northern origin near Dakar cannot be ruled out. In other words the concept of a wake, within which upwelled water in a confined northern area would simply be advected southward, may not be applicable. In that respect, the cold tongue may be distinct from upwelling filaments present in other upwelling sectors in which the key dynamical process is subduction of recently upwelled water as it flows offshore past the shelf break.

111 then within the range of influence of large slope/shelf break eddies and meanders whose surface
112 expressions are frequently seen impinging on the outer shelf (Ndoye et al. 2014). Such situations
113 occur preferentially between February and April and prevailed during our observational period².

114 The process underlying the offshore migration of the upwelling tongue is present and well un-
115 derstood in 2D across-shore/vertical (2DV) models. The key dynamical feature of 2DV models
116 subjected to upwelling favorable winds is the *upwelling front*. Under such idealizations the up-
117 welling front possesses several defining characteristics (Allen et al. 1995; Austin and Lentz 2002;
118 Estrade et al. 2008): it is the physical barrier between offshore non-upwelling and cold upwelling
119 waters, *i.e.*, it is the place of maximum surface density gradient (this can also be true for other
120 tracers); it is the place of maximum equatorward alongshore velocity; it coincides with the main
121 pycnocline outcrop (Austin and Barth 2002); low/vanishing stratification should be found on its
122 inshore flank, *i.e.*, the *upwelling zone* where cold interior waters are incorporated into the surface
123 layer.

124 Coalescence between the surface and bottom boundary layers has traditionally been invoked as
125 the main explanation for the displacement of the upwelling front away from the shoreline (Estrade
126 et al. 2008; Austin and Lentz 2002). In the alongshore momentum balance the maintenance of
127 well-mixed inner-shelf waters implies a compensation between wind and bottom friction with lit-
128 tle or no offshore Ekman transport needed. Therefore coastal divergence is expected to take place
129 where water is deep enough for the two boundary layers to separate, typically 15 to 40 m de-
130 pending in part on wind intensity (stronger winds lead to both thicker surface boundary layers and
131 thicker bottom boundary layers because they tend to increase the strength of the upwelling jet as

²The seaward displacement of the cold tongue is accompanied by the establishment of a nearshore warm water strip south of $\sim 14^{\circ}20'N$ that has historically attracted much attention because it is, intuitively, favorable to the retention of eggs and larvae of marine species (Demarcq and Faure 2000). The shallow and poorly charted area where this warm strip is found was considered unsafe for the R/V Antéa. Therefore, just a small number of observations were made at the edge of this strip which do not allow us to properly analyse its dynamics.

132 confirmed by observations described below). In the SSUC the migration of the upwelling tongue
133 on seasonal scales (very close to shore in the early season, farthest offshore in March when up-
134 welling winds are strongest and retreating back inshore in April-May) is consistent with the cycle
135 of upwelling wind intensity (Ndoye et al. 2014). On the other hand analysis of SSUC SST also
136 shows cold upwelling tongue behavior (in terms of zonal position and displacements) that is sug-
137 gestive of other processes being at play. Further north, over a wide continental shelf resembling the
138 SSUC, Barton et al. (1977) observe an upwelling front that migrates offshore during two consec-
139 utive upwelling events without any evident relation to changes in wind intensity. Similar behavior
140 will be described below for the SSUC. Overall, the connection between cross-shore migration of
141 the upwelling zone and wind intensity is unclear, at least on synoptic time scales.

142 The purpose of this study is to to better understand the dynamics underlying upwelling front evo-
143 lutions and, more generally, shed light on the dynamics of the SSUC. As we will see, other aspects
144 of 2DV conceptual model that have traditionally been used to investigate the SSUC dynamics need
145 serious reconsideration in the light of the UPSEN2/ECOAO observations. Identification of the up-
146 welling front during these experiments is frequently ambiguous and, when possible, the upwelling
147 front rarely satisfies all of the characteristics laid out above. Also, limited sampling of the inshore
148 edge of the upwelling tongue suggests that warmer coastal waters were overwhelmingly stratified
149 during the experiments, hence the 2DV view of the offshore migration of the upwelling tongue
150 does not seem to be relevant.

151 On the other hand, our observations provide multiple pieces of evidence pointing to the impor-
152 tance of complex scale interactions in the SSUC. In particular, shelf break/open ocean mesoscale
153 disturbances and superinertial dynamics (internal gravity waves in particular) exert a fundamental
154 influence on the SSUC dynamics, thermohaline structure and, in particular, on the position and
155 shape of the upwelling tongue.

156 The manuscript is organized as follows. Section 2 presents the data and methods. Section 3
157 describes the synoptic evolution of the SSUC state and circulation during the field experiments.
158 Emphasis is placed on the mid-shelf area where moored instruments allow us to better characterize
159 the dynamics. The flow regime and submesoscale activity are also briefly examined. In Section 4
160 a set of observations is presented from ship echosounders and moored instruments that suggests
161 the dynamical importance of the SSUC internal wave field. The final section summarizes and
162 elaborates on our findings and their consequences.

163 **2. Data and Methods**

164 *Moored Instruments*

165 A string of instruments (hereafter referred to as M28) was deployed in about 28 m water depth
166 at 14°N, 17°05'950W on 23 February (8 AM) and recovered on 12 March (3 PM). It consisted
167 of eight temperature (T) sensors and ten temperature, salinity (S) and pressure sensors with one
168 minute sampling interval. Measurements made by the 18 T sensors are used to obtain a temper-
169 ature time-depth gridded field (described in Sec. 3 and 4). This is achieved through objective
170 analysis (Bretherton et al. 1976), using 1 m and 2 mn for the vertical and time resolution of the
171 grid and 1 m and 4 mn for the decorrelation depth and time scale. The decorrelation time scale is
172 chosen so that internal wave signals with periods ~ 10 mn or more are preserved.

173 Three upward-looking ADCP moorings were also deployed 0.5 nm west and east (RDI 300 kHz
174 respectively referred to as RDIW and RDIE) and south (AQUADOPP 400 kHz; AQDS) of the
175 thermistor line. Mean water depth at the moorings ranged from approximately 29 m (RDIW) to
176 26.5 m (RDIE). One additional ADCP AQUADOPP 600 kHz was moored a few miles to the east
177 in 23m depth (AQDI). Deployment of the ADCPs took place on 22 Feb. between 10:20 AM and

178 12:10 PM. Recovery took place on 12 (RDIW) or 15 March. RDI (resp. AQUADOPP) ADCPs
179 sampled every 2 mn (resp. 5 mn) with vertical resolution of 1m. Accounting for the depth at which
180 the instruments head was located (≈ 0.5 m above ground) and a 1 m blanking distance the lowest
181 valid measurement is centered at 2m above the bottom. Because of side lobe reflection from the
182 air-sea interface the shallowest useable bin is centered at 5m depth. The barotropic component of
183 measured currents were detided using the software T_Tide (Pawlowicz et al. 2002). M2 is by far
184 the dominant constituent (not shown).

185 *Hydrographic Measurements*

186 Zonal (approximately across-shore) CTD transects were repeated at 14° , $14^{\circ}30'$ and $13^{\circ}40'$ N
187 during the surveys and additional yoyo CTD stations were also performed. Data were acquired
188 using a SBE911+, measuring redundantly pressure, temperature and conductivity at 24 Hz, and
189 fluorescence, oxygen at 2 Hz. Data postprocessing was performed using the seabird SBE pro-
190 cessing software and follows standard practices as described in many studies (see Morison et al.
191 1994 for example). Only the downcast profiles are used for analysis; during the upcast sensors
192 are in the wake of the package and CTD frame (Alford and Pinkel 2000). Raw pressure is filtered
193 using a 15 point triangle window. This is enough to eliminate all pressure reversals despite the
194 relatively low drop speed we chose to increase vertical resolution (0.5 m s^{-1}). We attribute this to
195 CTD operation through a moon pool located toward the center of R/V Antéa which limits heave
196 effects. Sea states were also favorable with limited swell in the area. A 5 point median filter is
197 applied to temperature and salinity. A correction for the conductivity cell thermal mass (Morison
198 et al. 1994) is also applied, requiring the knowledge of two parameters α (initial amplitude) and
199 τ (time scale) that characterize conductivity measurement error when instantaneously applying a
200 1° C step in temperature. SBE default values were checked and slightly modified using a series

201 of profiles exhibiting abrupt T jumps at the interface of a well-mixed 20-30 m thick bottom layer
202 (not shown). The salinity profile closest to a step was obtained for $\alpha=0.025$ and $\tau=7$ s and these
203 values are used for all CTD profiles. For most purposes including the construction of hydrological
204 transects, depth averaging is performed over 1 m bins. Bin size is reduced to 0.15 m to construct
205 yoyo CTD profiles used to estimate dissipation and mixing intensity, through the computation of
206 Thorpe scales (Sec. 4). This roughly corresponds to 7 scans at the drop speed of 0.5 m s^{-1} .

207 Alongtrack surface temperature and salinity are available from the SBE21 ship thermosalinome-
208 ter (TSG data hereafter).

209 *Ancillary Measurements*

210 R/V Antéa is equipped with a 4 frequencies scientific echo-sounder SIMRAD EK60 (38, 70,
211 120 and 200 kHz). Ping rate is 1 Hz which yields a 3.5 m native resolution for the echograms
212 when the ship steams at 8 knots.

213 The weather station onboard R/V Antéa (Batos 1.1D) provides wind speed and direction mea-
214 sured at approximately 20 m height. To minimize the effect of airflow distortion by the ship
215 superstructure, measurements corresponding to aft-wind conditions are systematically discarded.
216 Hourly wind at the Yoff weather station at Dakar Airport, Senegal ($14^{\circ}44'N$, $17^{\circ}30'W$, 27 m
217 above ground; hereafter DWS) are obtained from <http://www.ogimet.com/metars.phtml.en>. AS-
218 CAT scatterometers onboard METOP-A and B provide 2D wind measurements between 0 and 3
219 times a day, around 10:30 AM and/or 10:30 PM. We use the 12.5 km L2 products from NASA and
220 present these observations after spatial averaging over different subdomains of the SSUC.

221 We use L2 SWATH Moderate Resolution Imaging Spectroradiometer 'MODIS' onboard the
222 Terra and AQUA satellites distributed by NASA (<http://oceancolor.gsfc.nasa.gov>). The metric
223 ground resolution varies depending on view angle but remains close to the nominal 1 km value.

224 Cloud masking produces numerous false positives in upwelling regions and we instead rely on
225 visual examination over the SSUC to keep or discard images.

226 **3. Subinertial SSUC dynamics**

227 Several types of observations, presented below, give complementary perspectives on the physical
228 situation during the campaigns and, particularly, on the sequence of synoptic events.

229 *Synoptic variability*

230 DWS is generally quite representative of synoptic wind conditions over the SSUC, especially
231 in situations where northwesterlies dominate (Ndoye et al. 2014), as during UPSEN2/ECOAO.
232 Analysis of DWS wind records (Fig. 2a) suggest three coherent subperiods: a moderate relaxation
233 period RL1 from the beginning of the cruise (22 February) to 27 February when the wind over the
234 previous inertial period is back to above 5 m s^{-1} ; 28 February to 12 March (UP1) during which
235 the wind intensity remains essentially between 5 and 7 m s^{-1} ; and from 12 March to 17-18 March
236 during which another relaxation period RL2 takes place that, beside a more rapid initiation and a
237 longer duration (~ 5 days versus 3-4 days), resembles the earlier one RL1. The short upwelling
238 event that took place around 20-21 February just before UPSEN2 is referred to as UP0.

239 This description of DWS winds is broadly consistent with ship weather station observations
240 made within 50 km of M28 reported in Fig. 2d. For example, the weakest (respectively strongest)
241 ship winds are found on 25 February and 15 March (resp. 28 February and 8 March). This being
242 said, limited coverage at M28 and significant intradaily variability tend to overshadow the synoptic
243 signal and curtail a detailed comparison. In particular, daily wind cycles differ at M28 and DWS.
244 During most of the experiment upwelling wind intensity at M28 peaks in the evening or early at
245 night and is minimum around mid-day (Fig. 2e). Also note that upwelling events seem to manifest

246 themselves through increased maximum wind intensities at M28 while morning winds remain
247 generally weak. The daily wind cycle has a much lower amplitude at DWS and maximum wind
248 intensity occurs around 2PM (see Ndoye et al. 2014).

249 In Fig. 2b we show the zonal minimum temperature over the shelf averaged over the latitudinal
250 range 14° - $14^{\circ}30'$ N, computed for all cloud-free MODIS SST images (a subset of these images is
251 presented in Fig. 3). The upwelling event finished around the beginning of UPSEN2 UP0, the short
252 relaxation period RL1, central upwelling event UP1, and final relaxation RL2 are clearly identifi-
253 able as SST fluctuations of ~ 2 - 3° C. The termination date of RL1 cannot be determined precisely
254 in SST because no MODIS SST is available on 25 and 26 February, but declining temperatures on
255 27-28 February approximately coincide with the increase in upwelling wind intensity. As for the
256 SST warming during the late part of the observation period, its initiation around 8 March precedes
257 the marked wind drop on 12-13 March by around 4 days. We will come back to this discrepancy
258 when presenting mid-shelf variability. In SST RL2 is most marked on 17 March, *i.e.*, upon the
259 return of more favorable upwelling wind conditions.

260 Overall, the storylines based on DWS winds or synoptic evolution of the system SST are in
261 good agreement, considering the sampling limitations and complexity of the ocean response to
262 wind changes.

263 *SSUC mesoscale variability*

264 With over 50 nearly cloud-free images over the duration of the experiment, MODIS provides in-
265 valuable information on the state and synoptic variability of the SSUC at scales of a few kilometers
266 and larger.

267 Most images exhibit the patterns typical of the SSUC during the upwelling season, namely
268 the presence of a tongue of cold water whose source is situated just south of Dakar (where the

269 coldest waters are found) and extends southward over the shelf, with some warmer waters being
270 found offshore, but also inshore of the tongue south of $14^{\circ}30'N$. Southward attenuation of the cold
271 signal strongly varies with time.

272 During the entire experiment the frontal zone between the cold upwelling water and warmer
273 offshore water is distorted and forms filaments and meanders of typical size ~ 20 -100 km, some
274 of which acquire quasi-circular shapes (Fig. 3). As demonstrated for other upwelling systems these
275 mesoscale structures must be the manifestation of baroclinic-barotropic instability (Marchesiello
276 et al. 2003). The tendency of filaments to orient themselves along a NW-SE axis (Fig. 3e-h)
277 reflects the intense lateral shear (partly resolved by our across-shore sections, see below) between
278 the poleward Mauritanian current and the inshore equatorward upwelling flow.

279 In their analysis of the MODIS SST database Ndoye et al. (2014) identify a recurrent mesoscale
280 situation when a 30-100 km anticyclone (referred to as CVA for Cape Verde Anticyclonic struc-
281 ture) hugs the Cape Verde headland. In Feb.-March 2013 three different CVAs consecutively
282 occupy the northern SSUC following a sequence of events involving 1) northward propagation
283 and deformation/amplification of a Mauritania current meander initially situated further south;
284 2) phase-locking or reduced propagation of the meander which remains in the immediate vicin-
285 ity of the Cape Verde headland for several days while taking a more circular shape; 3) weaken-
286 ing/shrinking of the structure in a fashion that suggests mixing between warm waters in the CVA
287 core and colder waters.

288 At the beginning of UPSEN2 (21-23 Feb.) the remains of a small CVA (CVA-2) more easily
289 identified at earlier times (18 Feb., not shown) are still visible 50 km to the south/southwest of Cape
290 Verde (Fig. 3a). On 27 February (Fig. 4) the SST signal of CVA-2 has mostly faded. The SST scene
291 for 28 February (Fig. 3c) captures the transient situation when $\sim 18^{\circ}C$ water occupies the vicinity
292 of Cape Verde and warmer water is located ~ 30 km further offshore. It also reveals the final stage

293 of the evacuation of CVA-2 which has been stirred beyond recognition in the deformation region
294 near $17^{\circ}45'W$, $14^{\circ}45'N$; and the northward progression of the frontal edge oriented NW-SE that
295 separates a warm MC meander from upwelling water between $13^{\circ}40'N$ and $14^{\circ}50'N$ (compare
296 Fig. 3b and c). This frontal zone had remained quasi-stationary from 21 Feb to 24-25 Feb. By
297 3 March it has shifted considerably further north (Fig. 3d). It is then located partly north of and
298 in close contact with Cape Verde. The northern and southern parts of the front evolve somewhat
299 independently thereafter. North of Cape Verde, the front progresses northward and forms a barrier
300 to cold upwelled water (Fig. 3e), even right at the coast where SST are systematically warmer than
301 $20^{\circ}C$ during UP1. South of Cape Verde the front combines with a $\sim 20^{\circ}C$ water filament located
302 at $17^{\circ}45'-18^{\circ}W$ to form the quasi-circular edge of a mesoscale structure (CVA-3) between 5 and
303 10-12 March (Fig. 3e,f).

304 The SST signature of CVA-3 is progressively eroded, particularly at its eastern side as seen
305 on 12 March (Fig. 3f). On 14 March (Fig. 3g) the remains of CVA-3 are barely visible as a
306 bulge of $\sim 20^{\circ}C$ water near $17^{\circ}45'W$, $14^{\circ}30'N$. Later on during RL2 (Fig. 3h,i) SST images
307 reveal a major reorganization of the flow structure in the vicinity of the Cape Verde peninsula.
308 The upwelling signature on SST is confined to the northern SSUC (note that the maintenance of
309 some upwelling is consistent with DWS and ship wind records, see Fig. 2). The orientation of
310 the wake of waters upwelled at the Cape Verde peninsula suggests that the surface flow is directed
311 offshore on 18 March in the region between the coast and a subsequent warm meander still situated
312 approximately 50 km offshore to the southwest (Fig. 3i). VIIRS ocean color images available for
313 17 and 18 March further support the onset of an offshore surface flow in the northern SSUC toward
314 the end of RL2 (not shown).

315 The mesoscale features described above are typically located over the continental slope but they
316 also frequently extend onto the shelf as described below using in situ observations. Their evolution

317 is tied to that of the SSUC cold tongue over the shelf, *e.g.*, through upwelling filaments. Pending
318 modeling sensitivity analyses our conceptual view of the SSUC dynamics is that offshore and
319 shelf dynamics are coupled through the instabilities of the shelf/shelf break/slope current system.
320 Synoptic variability of the MC transport and of the wind-induced shelf circulation are a priori
321 important sources of modulation for these instabilities.

322 *Subsurface properties and thermohaline structure*

323 The set of CTD casts carried out during the experiments offer important subsurface information.
324 In particular they allow us to examine the properties of the cold subsurface water that feeds the
325 upwelling and its relation to SST. Stratification is also useful as a signature of mixing. Fig. 5
326 represents the across-shelf distribution of temperature, salinity, dissolved oxygen and fluorescence
327 in the bottom layer, and surface to bottom density difference. Figs. 6 and 7 represent T and S along
328 thirteen of the 17 main cross-shore transect lines.

329 All transects exhibit the signature of cold (14-15° C) and fresh bottom water, with low dis-
330 solved oxygen and fluorescence properties, rising up the shelf to feed the Ekman divergence. T-S
331 properties and, in particular, low subsurface salinity are typical of the south Atlantic central water
332 (Hughes and Barton 1974; Peña-Izquierdo et al. 2012). A remarkable trait of this signature is that
333 it tends to fade away when approaching the shore, although to various degrees depending on the
334 transect and the tracer. The southern transects (T4, T9 and to a lesser extent T14) exhibit the most
335 pronounced changes in bottom water T,S properties across the shelf. The northern transects (at
336 14° 30'N) T1 and T12 are those where bottom water T,S properties are best preserved. Although
337 this does not apply to T8 it confirms the visual impression from the SST images that the shelf is
338 preferentially fed with slope waters in the northern SSUC. Many studies document the effect of
339 capes and changes in shelf width on upwelling pathways and strength, which adds support to the

340 visual impression (Gan and Allen 2002; Pringle 2002; Pringle and Dever 2009; Gan et al. 2009;
341 Crépon et al. 1984). Ongoing modelling work specific to the area is also supportive of this (Ndoye
342 2016).

343 The cross-shelf changes in tracer properties strongly depend on the tracer itself. Salinity con-
344 tributes very little to density spatio-temporal variability (see Fig. 5f) but its fluctuations over the
345 shelf are nonetheless measurable and provide useful indications on mixing. Salinity and tem-
346 perature experience marked relative changes between the shelf break and the 15 m isobath. The
347 changes are most pronounced over the outer shelf for salinity with a tendency to saturation at
348 about 35.6 psu for depths shallower than 40-50 m (Fig. 5b). The cross-shore structure is reversed
349 for temperature with the most significant changes occurring at depths shallower than 30 m. How-
350 ever the warming trend from deep to shallow parts of the shelf is ubiquitous. For dissolved oxygen
351 changes are very limited at depths greater than ~ 30 m and generally consist in a slight reduc-
352 tion from offshore to nearshore. For shallower depths a large variability is found, particularly at
353 the central and southern transects. Changes in fluorescence resemble those for oxygen although
354 they are less concentrated to the shallowest depths, *e.g.*, the outer shelf variability is much more
355 pronounced.

356 Modification of bottom water biogeochemical properties when getting closer to shore goes in
357 pair with a reduction in surface to bottom stratification (Fig. 5e,f), which occasionally vanishes in-
358 shore of the 30 m isobath. This points to the importance of vertical mixing as a process controlling
359 the distribution of water column properties. Other processes shape the mean tracer distribution and
360 in particular sources and sinks. We presume that biological activity is able to maintain sharp verti-
361 cal contrasts in oxygen and fluorescence between the upper 20-40 meters and the layer below and
362 prevent mixing from significantly affecting the vertical distribution of these two tracers. For ex-
363 ample, ventilation through mixing is unable to prevent hypoxia from developing toward the end of

364 ECOAO during the relaxation period (see the three low dissolved oxygen outliers in Fig. 5c). This
365 and other synoptic anoxic/hypoxic events are under investigation, similarly to what is being done
366 in other upwelling regions, Adams et al. 2013). Conversely, the absence of interior source/sink for
367 temperature and salinity allows vertical mixing to have a significant impact on these fields.

368 Other aspects of the SSUC thermohaline structure suggest the importance of mixing. As men-
369 tioned in the introduction the key dynamical feature of idealized upwelling models is their well-
370 identifiable upwelling front, located where the main pycnocline outcrops and separates upwelling
371 and non upwelling waters. The complexity of the SSUC upwelling structure leads to equivocal
372 situations regarding the definition/localization of the upwelling front and zone. In particular the
373 surface temperature and salinity across-shore gradients are frequently weak and diffuse, *e.g.*, 2° C
374 over 25 km for T1, from CTD6 to CTD12. A notable exception is found during T6 (14°N) where
375 a 1.4° C change was observed over a horizontal distance of 250 m. Other exceptions are described
376 in details below as part of a submesoscale activity analysis.

377 More importantly, choosing a density/temperature value characteristic of the offshore pycnocline
378 and following it toward the coast to its outcropping position does not reliably help define the lo-
379 cation of the upwelling front, in contrast to, *e.g.*, what happens over the Oregon shelf (Austin and
380 Barth 2002). The main reason for this is that considerable changes in stratification and thermo-
381 haline structure occur across the shelf, not just in the bottom layer as described above but also at
382 mid-depth. Manifestations of intense mixing of thermocline waters include the presence of bulges
383 of water in temperature classes that are almost unrepresented offshore (CTD43 in T4, CTD55-56
384 in T5, CTD70 in T6, CTD108-111 in T10, CTD163 in T15).

385 In other words, except at the northern transects T1, T8 and T12 (which exhibit clear upwelling
386 frontal structures as found, *e.g.*, offshore of Oregon in Huyer et al. 2005) and at the southern T14
387 (which resembles the idealized 2DV upwelling in Estrade et al. 2008 and Austin and Lentz 2002)

388 the exact location where upwelling is taking place is difficult to identify precisely. For example,
389 T6 has a strong surface temperature gradient and an almost well mixed water column at 17°10'W
390 but a significant amount of cold bottom water resides inshore of that location. A more dramatic
391 example is obtained for T15 at the end of upwelling event UP1. On 12 March the upwelling front
392 location at 14°N, determined as the place of zonal minimum SST (from MODIS SST in Fig. 2c
393 or TSG data, not shown), sits around 17°25'W in 75 m water depth near CTD 163. On the other
394 hand, a secondary SST minimum (see Fig. 2c) is found much closer to shore near M28 and cold
395 bottom water resides over most of the shelf, including at mooring M28 (see Fig. 8).

396 We attribute this complexity of the shelf thermohaline structure properties to intense vertical
397 mixing. Although bottom friction may be also implicated we present evidence that internal gravity
398 waves breaking should play an important role as a source of mixing in Sec. 4.

399 *Mid-shelf dynamics*

400 The description above can be complemented by and contrasted with the continuous current and
401 temperature measurements available at 14°N about the 28 m isobath, although records cover a
402 restricted period from 23 February to 12 or 15 March. In what follows, heat content is defined as
403 $\int_{z_b}^{z_s} \rho C_p (T - T_m) dz$ where C_p is the heat capacity of water taken equal to 3985 J kg⁻¹ °C⁻¹, T_m
404 is the mean vertical profile of temperature at M28 over the measurement period, and the integral
405 goes from 5 to 27 m depth.

406 Heat content and stratification at M28 are mainly consistent with SST evolution there (or more
407 broadly over the shelf), *i.e.*, they roughly follow the wind conditions. Heat content (Fig. 8c) under-
408 goes a large increase from 25 to 27-28 February during RL1 and a rapid decrease on 28 February
409 - 1 March at the beginning of UP1. Changes before the 25th or after 1 March are comparatively
410 modest in amplitude and rate but an upward trend is noticeable from 2 to 8 March and 10 to 12

411 March, with a fall-off between these two periods. Assuming that only air-sea exchanges contribute
412 to the heat content increases during RL1 would imply a net air-sea heat flux of $\gtrsim +200 \text{ W m}^{-2}$
413 (see Fig. 8c), not inconsistent with climatological air-sea heat fluxes in late February/early March
414 from COADS (140 W m^{-2} , Woodruff et al. 1998), OAflux (105 W m^{-2} , Yu and Weller 2007), or
415 CFSR reanalysis (120 W m^{-2} , Saha et al. 2010). During UP1 onset phase a similar assumption
416 would imply unrealistic heat losses of the order of -400 W m^{-2} and lateral advection is thus nec-
417 essarily implicated in the drop. Largest temperature changes are near the surface (Fig. 8f) where
418 currents are about 3 times stronger than near the bottom (~ 25 versus $7\text{-}10 \text{ cm s}^{-1}$, see Fig. 9).
419 This strongly suggests that a key term driving M28 heat content evolution in the beginning of UP1
420 is near-surface southward advection of cold water upwelled in the northern SSUC.

421 Daily and intradaily fluctuations are also present in the heat content signal particularly during
422 the early (23-28 March) and to a lesser extent late (10-12 March) phases. The time scale of the
423 fluctuations span a wide range of scales but periods of ~ 20 mn or less dominate and reflect the
424 importance of nonlinear internal waves (see next section).

425 Near-surface to bottom stratification evolution on synoptic time scales is similar to heat content
426 although, at the onset of UP1, it peaks about one day before on 26 March and drops more rapidly
427 (Fig. 8d). We relate this to differences in the controlling processes. Indeed, the return of stronger
428 winds enhances 3D turbulence levels and may erode stratification on a time scale of hours (two-
429 hourly averaged winds reach 13 m/s on the evening of 27 February which yields an increase in
430 sustained maximum stress by 40% - resp. 100% - in comparison to 26 - resp. 25 - February).
431 In contrast, changes in heat content should be more progressive because enhanced winds reduce
432 air-sea heat fluxes by a few tens of W m^{-2} only (given the range of wind fluctuations between
433 RL1 and UP1) and changes in lateral advection of cold waters should require one inertial period
434 or more to be felt (Csanady 1982).

435 Non-zero stratification ($> 0.5^{\circ}$ C difference between top and bottom thermistors) is maintained
436 during most of UP1. This is despite the fact that the mooring is located inshore of the main
437 upwelling front during that period, as revealed in CTD transects T6 on 26 February, T10 on 2
438 March and T13 on 7 March (see Fig. 6 and Fig. 7). There are only two brief moments when the
439 water column is fully mixed or very near so, on 1 and 7 March. Winds measured by the ship at
440 these times near M28 are the strongest observed during the entire period (Fig. 2d).

441 Bottom temperature evolution during the early UP1 period (between 26 February and 1 March)
442 shows a pronounced increase $\sim 0.5^{\circ}$ C. This suggests that the initial response to increasing winds
443 (enhanced vertical mixing) remains perceptible for 3-4 days at M28. Alternatively, warmer bottom
444 waters may have been present north of M28 and the temperature evolution would simply result
445 from their southward advection but T5 and T8 temperature sections (Fig. 6) are not particularly
446 supportive of this.

447 More generally, bottom temperature evolution at M28 illustrates the slow and complex response
448 of bottom layer properties to the upwelling wind history: coldest bottom temperatures coincide
449 with the maximum relaxation during RL1 and also with the very end of UP1 and onset of RL2 (the
450 return of bottom water as cold as that found on 25 February only occurs on 10 March). Conversely,
451 warmest temperatures are found after 8 days of sustained upwelling at the time when coldest
452 surface temperatures are recorded in the system (Fig. 2b). The long inertial time period (of the
453 order of two days at the SSUC latitude) and, most importantly, the shelf width are two important
454 factors that must contribute to the delays and decouplings between the onset of an upwelling-
455 favorable wind event, cold water flowing over the shelf break, and that water reaching the M28
456 mid-shelf region. In turn, because the flushing of shelf bottom waters must take more time than,
457 *e.g.*, relaxation RL1 lasts, the shelf thermohaline structure integrates the history of a succession of
458 upwelling events (such as UP0 and UP1).

459 Mid-shelf alongshore currents (Fig. 9 at RDIE) essentially reflect the same RL1/UP1/RL2 suc-
460 cession of events with northward flow around 26 February and toward the end of the period (note
461 that northward surface flows are only found in the core of RL2 with maximum intensity 0.1 m
462 s^{-1}). Southward flow prevails in between, with two surface peaks at approx. 0.4 m s^{-1} in con-
463 junction with the well-mixed conditions on 1 and 7 March. Some important flow subtleties can
464 also be noted.

465 Most unexpectedly, a weak relaxation of the southward flow at RDIE stands out from 3 to 5
466 March. Alongshore currents do not reverse at RDIE but they do at RDIW and AQDI where the
467 northward flow remains modest nonetheless, below 5 cm s^{-1} (not shown). Because the ship was
468 not at sea during this time period, we lack contextual information to interpret these changes but we
469 note that wind intensity reduced slightly after 1 March (Fig. 2a) which may have been sufficient
470 to trigger the southward flow relaxation. A similar explanation may be invoked to explain the
471 timing of the alongshore current relaxation initiated around 9 March, *i.e.*, several days prior to the
472 major RL2 wind drop but coincident with a limited wind reduction seen in DWS and ship atmo-
473 spheric measurements (Fig. 2a and d). As noted previously, SST also suggests a RL2 initiation on
474 9 March, as opposed to 12 March when DWS winds strongly relax (see above). The wind drop
475 around 8-9 March is limited however (10 % in meridional wind intensity at DWS, 30 % in wind
476 stress). Available satellite SST images offer additional insight into this early onset of RL2. In
477 Fig. 3f we have represented the position of the 20° C isocontour about two days prior to that scene
478 at 11 PM on 9 March. The change in contour location between 10 and 12 March suggests that
479 flow relaxation/reversal over the mid-shelf during that period is part of a larger scale tendency to
480 northward advection. Whether the displacement of the slope mesoscale features is part of the re-
481 sponse to a limited wind drop or is the cause of an early flow relaxation cannot be determined with

482 the observations at our disposal. Below, mesoscale activity will be more convincingly implicated
483 as a direct cause of another synoptic flow fluctuation taking place over the shelf.

484 Cross-shore velocity evolutions have generally been more difficult to interpret than alongshore
485 ones (Lentz and Chapman 2004). Subsurface cross-shore velocities are directed onshore during
486 the entire UP1 period but also during RL1. During the first part of RL2 when RDIE is still moored
487 the current alternates between onshore and offshore with a period ~ 2 days suggestive of near-
488 inertial oscillations (Millot and Crépon 1981). Cross-shore velocities in the surface boundary
489 layer are essentially directed offshore. They are strongest during UP1 except for a short inversion
490 to onshore coincident with the second time period when the water column is fully destratified.
491 The first destratification episode on 1 March also coincides with reduced offshore flow near the
492 surface. In both cases enhanced turbulent vertical diffusion of momentum at times of intense wind
493 mixing are likely responsible for the anomalous onshore surface flow.

494 The largest cross-shore velocities are found at mid-depth on 26-27 February, *i.e.*, at a time
495 when winds have started to increase moderately at DWS (wind evolution at M28 is less clear,
496 see Fig. 2a and d) and the alongshore flow is not established to equatorward yet. The duration
497 of this onshore pulse is too long to be consistent with a wind-induced inertial oscillation. An
498 alternative explanation is suggested by the sequence of MODIS SST images for 24,27 and 28
499 February (Figs. 3b,c and 4). These images offer a detailed view of the mesoscale activity and
500 its evolution during that period. On 27-28 February a warm MC meander that will subsequently
501 form CVA-3 impinges on the shelf with its edge reaching the 30 m isobath. Comparison with
502 the image for 24 February indicates that a rapid displacement of the meander crest toward the
503 northeast (*i.e.*, toward the mooring area) has taken place over 2-3 days. Concomitantly, the cold
504 upwelling tongue undergoes a noticeable shoreward displacement (followed by a rapid offshore
505 retreat). On 27 February it occupies a zone inshore of M28 at 14°N (Fig. 4). The existence of a

506 short-lasting onshore advection episode is also consistent with temperature observations at M28
507 where a substantial lateral flux contribution is required to explain the heat content increase around
508 that day (Fig. 8c).

509 Because R/V Antéa steamed multiple times across the mid- and outer-shelf in the latitude range
510 14° - $14^{\circ}10'$ N between 26 February 3AM and 28 February 0:30 AM, additional observations are
511 available to support the existence of a shelf-wide event of onshore flow driven by mesoscale ac-
512 tivity. A cross-section of (u,v) velocities is obtained by averaging the ship ADCP measurements
513 made during these transects. Data are binned using the native resolution of the ADCP in the ver-
514 tical (8 m bins, the uppermost one being centered at -19 m) and a 0.025° mesh size in longitude.
515 The ADCP configuration used 5 min ensemble averaging. All the ensembles for a given transect
516 falling into one 0.025° longitude bin are pre-averaged and contribute for only one observation. We
517 did not try to weight the transects so as to minimize the influence of tidal currents (*e.g.*, as done
518 in Avicola et al. 2007) but we have verified that tidal phases are such that substantial canceling
519 is happening in the averaging (which is only important for u given the shape of tidal ellipses, not
520 shown). The result is shown in Fig. 4a,b and allows us to place the mooring observations around
521 27 February in a broader across-shore perspective. During this period subsurface currents over
522 most of the shelf are toward the northeast. Onshore velocities reach 20 cm s^{-1} over the outer shelf
523 with a maximum positioned at mid-depth. Onshore velocities remain $\sim 10 \text{ cm s}^{-1}$ as close to
524 shore as the ship ADCP can measure. Closer to shore RDIW and RDIE zonal velocities are also
525 around 10 cm s^{-1} . Inspection of all available ship ADCP transects near 14° N confirm the unusual
526 intensity of this onshore flow. Intense poleward currents as those depicted in Fig. 4b are more
527 commonly observed, although they are generally confined to the slope and outer shelf area.

528 SST images during the UPSEN2/ECOAO (and at other times) clearly show the frequent incur-
529 sion of MC mesoscale meanders and eddies onto the shelf. These are presumably the manifes-

530 tations of instability modes for the system formed by the poleward current and the equatorward
531 upwelling flow. Based on the discussion above, we see the episode of onshore flow on 26-27
532 February as related to such a mesoscale event. The unstable behavior of a shelf/slope current
533 system has recently been studied in the downwelling case (Wang and Jordi 2011). Our observa-
534 tional results highlight the need to perform a similar study in the context of upwelling systems.
535 This would help explore and clarify the interactions between the shelf upwelling jet and the slope
536 current, the influence of the wind in modulating these interactions, and most importantly, the con-
537 ditions under which mesoscale perturbations penetrate deeply into the shelf.

538 *Flow parameters and regime*

539 Several important flow characteristics can be derived from the observations and analyses pre-
540 sented in the previous section, with the objective to compare the SSUC to other upwelling regions.

541 From Fig. 5e, the Brunt Väisälä frequency can be computed at every CTD station. Ignoring a
542 few outliers, we find relatively uniform values for $N \approx 10^{-2} \text{ s}^{-1}$ which yields deformation radius
543 values ranging from $\approx 8 \text{ km}$ at mid-shelf to 27 km at the shelf break, *i.e.*, on the higher end of what
544 is typically found in upwellings. This is mainly because the Coriolis parameter is small ($f = 3.6 \times$
545 10^{-5} s^{-1} at $14^\circ 30' \text{ N}$). The topographic slope along all three transects is also quite uniform $\alpha \approx$
546 2×10^{-3} . The resulting slope Burger number $S = \frac{\alpha N}{f}$ is around 0.5. In a steady 2D upwelling, the
547 way the return onshore flow balancing offshore Ekman transport is achieved depends on S (Lentz
548 and Chapman 2004). S smaller (resp. greater) than 1 implies that the wind stress is balanced by
549 bottom friction (resp. nonlinear across-shelf flux of alongshore momentum) so the return flow
550 is concentrated in the bottom boundary layer (resp. distributed in the water column below the
551 surface boundary layer). $S = 0.5$ suggests the importance of frictional forces in the alongshore
552 momentum balance but is comparable to values found offshore of Oregon and northern California,

553 where both the topographic slope and Coriolis frequency are larger (Lentz and Chapman 2004).
554 The prominence of the cold bottom layer rising up the shelf in most TS transects (Fig. 6 and 7) is
555 qualitatively consistent with this.

556 Geostrophy is an important force balance that the non-tidal part of the flow should approximately
557 satisfy. Tidally filtered RDIE currents at M28 described above exhibit substantial fluctuations on
558 time scales of 1 day or less, particularly in the alongshore direction (Fig. 9). This suggests that
559 deviations from geostrophy are important and the subinertial flow is characterized by Rossby num-
560 bers that are not negligibly small compared to 1. Because wind fluctuations do not conclusively
561 explain several rapid flow changes we tend to see this as a manifestation of the submesoscale
562 dynamics in the upwelling zone.

563 Submesoscale turbulence consists of fronts, small eddies and filaments with typical horizon-
564 tal scales $\lesssim R_d$ (where R_d is the first deformation radius) and a strong tendency to near-surface
565 intensification. Key processes for submesoscale generation are (Capet et al. 2008e) i) strain-
566 ing/frontogenesis by mesoscale structures which intensifies pre-existing buoyancy contrasts and
567 leads to fronts whose vertical scale is typically that of the mesoscale ii) straining/frontogenesis
568 by fine-scale parallel flow instabilities which distorts mesoscale buoyancy gradients and produces
569 submesoscale flows whose vertical scale can be much smaller than that of the mesoscale. An
570 archetypal example of ii) is mixed layer baroclinic instability which generatew submesoscale
571 flow fluctuations approximately confined into the mixed layer (Boccaletti et al. 2007; Capet et al.
572 2008e). In their most extreme manifestations, contrasts across submesoscale fronts can reach
573 several degrees over lateral scales of 50-100 m. Such contrasts are the consequence of intense
574 straining in situations where diffusion is weak.

575 Upwelling dynamics are well-known to induce intense submesoscale frontal activity but some
576 precision is in order to connect with our SSUS study. Submesoscale fronts are ubiquitous in the

577 offshore coastal transition zone where cold upwelled and warm offshore waters are being mixed
578 (Flament et al. 1985; Capet et al. 2008d; Pallàs-Sanz et al. 2010). Our study is concerned with shelf
579 dynamics where the interaction between cold upwelling and warmer offshore waters is strongly
580 constrained by topography, friction, and inertia-gravity wave breaking. A numerical investigation
581 of the northern Argentinian shelf dynamics indicates that submesoscale is strongly damped in
582 water depths shallower than ~ 50 m (Capet et al. 2008a) and the same should apply to the SSUS,
583 hence we expect limited submesoscale turbulence over the inner- and mid-shelf. On the other
584 hand, the upwelling front is frequently located over the outer shelf where it can be subjected to
585 straining by CVAs so it is a priori conducive to the formation of submesoscale features.

586 To explore this possibility, we use TSG temperatures from multiple across-shelf transects con-
587 ducted between 9 and 10 March at 14° and $14^\circ 05'$ N, a subset of which is presented in Fig. 10.
588 Temperature contrasts across the upwelling front are clearly modulated at scales of a few hours
589 and less than 10 km in the alongshore direction, *i.e.*, at submesoscale. Temperature differences
590 of $\sim 1\text{-}2^\circ$ C over 100-200 m are found (two bottom panels in Fig. 10) and must reflect localized
591 straining and frontogenesis. At earlier times temperature changes are much smoother. A process
592 that might be responsible for such modulations would be the submesoscale destabilization of the
593 upwelling front with alternating frontogenesis and frontolysis in relation to crests and troughs of
594 unstable waves (Spall 1997). Some of the satellite images are consistent with this (Fig. 3b, see
595 the two filamentary regions around $17^\circ 15' \text{W}$, $13^\circ 15' \text{N}$ and $13^\circ 45' \text{N}$) but submesoscale distortions
596 of the upwelling front are modest and infrequent compared to observations for other regions (see
597 Fig. 16 in Capet et al. 2008e or Fig. 3c in Capet et al. 2008a) scenes in Fig. 3). Over most images
598 front sharpness has evident alongfront variations but these variations are more commonly at the
599 mesoscale (Fig. 3a,c,e Fig. 4 top) in relation with straining by CVAs, hence process i) seems more
600 important than process ii). This may be otherwise during periods where stronger winds and pos-

601 sibly detabilizing air-sea heat fluxes lead to deeper mixed layers and thus more energetic subme-
602 soscale instabilities (Fox-Kemper et al. 2008). Note that we see no signs of subduction/upwelling
603 at the upwelling front but we lack high resolution subsurface measurements that would allow us
604 to observe their fine-scale signature, *e.g.*, on biogeochemical tracers (Evans et al. 2015). Note also
605 that preferential but intermittent internal wave dissipation/mixing in the vicinity of the upwelling
606 front could well contribute to the alongfront modulations of its sharpness (see next section).

607 **4. The SSUC internal wave field**

608 Internal gravity waves are well known contributors to mixing in the coastal ocean. The accepted
609 view is that internal tides generated at the shelf break tend to evolve nonlinearly and give rise to
610 shorter-scale internal waves as they propagate nearshore. Steepening and breaking (Moum et al.
611 2007, 2003; Lamb 2014) is inherent to the propagation toward shallower waters but the subinertial
612 environment can also enhance dissipation, *e.g.*, through mutually reinforcing shears as found by
613 Avicola et al. (2007). This latter study indicates that, over the Oregon shelf, internal wave breaking
614 has a modest impact on vertical fluxes of tracers, a conclusion also reached by Schafstall et al.
615 (2010) for the central Mauritania outer shelf region, just a few degrees north of the SSUC.

616 Isolated satellite measurements suggest that the SSUC is also subjected to IGW wave activity
617 (*e.g.*, Jackson and Apel 2009). In this section we describe circumstantial evidence that SSUC
618 IGW activity was ubiquitous during UPSEN2 and ECOAO and that its intensity was at times very
619 strong. Because we did not have any microstructure sensor onboard, no direct local dissipation
620 estimates are available. On the other hand, our observations point to the importance of mixing, not
621 only near the bottom where frictional effects may be implicated but also in the intermediate part
622 of the water column where significant water mass transformation is revealed by several CTD casts
623 (Figs. 6 and 7, *e.g.*, CTDs 55-56 in T5; 108-111 in T10). In addition, mid-shelf observations from

624 moored instruments are used to estimate the energy associated with wave packets, which seems
625 enough to influence the evolution of the upwelling front region.

626 *Circumstantial evidence*

627 Antéa is equipped with a 4 frequencies EK60 echosounder (see Sec. 2). Inspection of all available
628 echograms indicates ubiquitous nonlinear internal wave activity over the southern Senegal shelf.
629 During UPSEN2, these waves manifest themselves as depressions of the main thermocline located
630 in the vertical at about 1/3 of the water depth. Maximum crest to trough amplitude frequently
631 reach 40 m or more over the outer shelf (see Fig. 11). Short internal waves (wavelengths of a
632 few hundred meters) are embedded into longer waves (wavelengths around 10 km) as in situations
633 where internal tides undergo fission (Gerkema 1996; Li and Farmer 2011).

634 Beside visual resemblance between the patterns exhibited in Fig. 11 and commonly observed
635 internal gravity waves, both yoyo CTDs and Scanfish observations at constant depth confirm that
636 echograms reflect displacements of the thermocline associated with time periods of a few minutes
637 and amplitudes of tens of meters. Several yoyo CTDs were performed in the hope that they would
638 help quantify mixing intensity. One took place on 25 February at 14°N, 17°20'W in about 60 m
639 water depth as the leading edge of an internal tidal wave passed that location (Fig. 12a). A Thorpe
640 scale analysis is performed on the 17 downcast profiles, following Thompson et al. (2007). Note
641 that Thorpe scale analysis is only valid when horizontal density gradients can be neglected (Dillon
642 1982). TSG data obtained immediately prior to the yoyo station provide a useful estimate of
643 the horizontal density gradients in the station vicinity. Density gradient is smooth and relatively
644 constant in the area with a typical maximum value for $\frac{g}{\rho_0} \partial_x \rho$ around $2.5 \times 10^{-6} \text{ s}^{-2}$. Thorpe
645 overturns with N^2 lower than twice this value will be put aside. Dominant vertical gradients in
646 salinity are by far those associated with spikes induced by thermal lag in the conductivity sensor.

647 On the other hand, salinity has a minor effect on density gradients, both horizontally and vertically
648 with a salinity range whose amplitude is systematically below 0.2-0.25 psu over the entire shelf,
649 *i.e.*, equivalent to $\sim 1^\circ$ C in its effects on density (see Fig. 5f). By comparison, temperature
650 gradients are 4-5 times stronger. As in Alford and Pinkel (2000) we therefore compute Thorpe
651 displacements and overturn scales based on temperature alone (see Fig. 12b-d). Finally, note that
652 estimates of vertical diffusivity K_v are computed assuming constant mixing efficiency $\gamma = 0.2$.
653 The weakly stratified upper layer is where the largest Thorpe displacements and dissipations are
654 found (as in Moum et al. 2007) with values occasionally reaching 10^{-5} W kg $^{-1}$. Vertical diffu-
655 sivity values are also very large, in the range 10^{-3} - 10^{-2} m 2 s $^{-1}$. Weaker dissipation maxima \sim
656 10^{-7} W kg $^{-1}$ are found in the lower half of the water column at that particular station. Mid-depth
657 ϵ one order of magnitude larger are obtained for one profile (not shown) carried out in the vicinity
658 of CTD 89 (transect T8) where both temperature and salinity show conspicuous signs of interior
659 mixing (see Fig. 6). Overall, interior K_v values are frequently in the range 5×10^{-5} - 5×10^{-3}
660 m 2 s $^{-1}$ but they are most often associated with overturns at the margin of detectability with stan-
661 dard CTD measurements. More sophisticated methods will be needed to characterize and quantify
662 the intensity of localized mixing episodes induced by internal gravity waves and their relationship
663 with the shelf environment (Walter et al. 2014; Palmer et al. 2015).

664 *Mid-shelf IGWs and their effect on the upwelling front*

665 A different approach to quantify the effect of IGW mixing relies on bulk estimates of IGW
666 dissipated power over portions of the shelf (Jeans and Sherwin 2001). Depending on the SSUC
667 thermohaline structure a given fraction of the energy converted to baroclinic tides at the shelf
668 break is able to propagate nearshore to the mid-shelf area. Sampling intervals of 2 moored ADCPs
669 (2 mn for RDIW and RDIE) and thermistors mounted on M28 (1 mn) are adequate to resolve

670 IGW activity when it is present. For example, the signature of wave packets is visible at M28 in
 671 temperature, mainly before 28 February and to a lesser extent after 10 March (Fig. 8).

672 In the remainder of the section, mooring data are used to compute 1) internal gravity wave
 673 energy at that location and, under some assumptions, 2) how much mixing can be achieved in the
 674 mid-shelf area where that energy can dissipate.

675 Given the observations at hand we choose to estimate the IGW energy flux F^w passing through
 676 M28 as $c_g \times (EKE^w + APE^w)$ where c_g is the speed at which wave trains propagate in the area and
 677 EKE^w (resp. APE^w) is the depth integrated kinetic (resp. available potential) energy associated
 678 with IGWs. This requires the definition of a low-pass operator $\bar{\cdot}$ such that high-pass deviations
 679 (denoted with a prime) adequately capture the flow and thermohaline fluctuations corresponding
 680 to IGW activity. We use a running mean with flat averaging over time intervals of duration T_{lf}
 681 longer than the internal wave period for $\bar{\cdot}$.

682 APE^w is quantified using the approach valid for arbitrary stratifications detailed in Holliday and
 683 McIntyre (1981) (see also Roulet and Klein 2009 and Kang and Fringer 2010):

$$APE^w(t) = \int_{-H}^0 \left[\int_{z_r(\rho(z,t),t)}^z g(\rho - \rho_r^w(z',t)) dz' \right] dz \quad (1)$$

684 where $\rho_r^w(z,t)$ is the density profile of the reference state, $z_r^w(\rho)$ its bijection, *i.e.*, the equilibrium
 685 depth of a parcel of density ρ . Density reference states are determined by reordering density
 686 observations over overlapping time intervals of duration T_{lf} . Each resulting reference state is
 687 then used to compute $APE^w(t)$ over a time subinterval of size T_{sub} smaller than T_{lf} (to limit edge
 688 effects). Choosing T_{lf} in the range [0.5 3] hours and T_{sub} from 1/3 to $1 \times T_{lf}$ does not reveal
 689 important sensitivities of either APE^w or EKE^w estimates. We present results for $T_{lf} = 30$ mn and
 690 $T_{sub} = 15$ mn.

691 EKE^w is quantified as

$$EKE^w(t) = \frac{1}{2}\rho \int_{-H}^0 (u'^2 + v'^2 + w'^2) dz - EKE^{bg} \quad (2)$$

692 In this definition EKE^{bg} represents the non zero background value of the high-pass eddy kinetic
693 energy found even during the period when the mooring is located inshore of the upwelling front
694 and fast motions may be due to other processes than internal gravity waves that we wish to exclude
695 from the analysis, including instrument noise . Based on Fig. 14 a conservative value for EKE^{bg}
696 is 24 J m^{-2} . In practice, vertical integration ranges for APE^w and EKE^w are restricted to where
697 valid observations are available (see Sec. 2).

698 To determine c_g we estimate the delay between the arrival of particularly identifiable wavetrains
699 at RDIW, M28 and RDIE. This method has inherent uncertainties because the wavetrains can be
700 significantly modified, particularly between RDIW and RDIE which are separated by $\sim 1 \text{ nm}$.
701 c_g values are in the range $0.18\text{-}0.30 \text{ m s}^{-1}$. For the wavetrain shown in Fig. 13 the estimation
702 is quite accurate between M28 and RDIE (despite inconsistencies prior to the arrival of the main
703 wavepacket, see Fig. 13). It yields $c_g = 0.25 \text{ m s}^{-1}$, a central value we retain for further use below.
704 Incidentally, Fig. 13 also suggests the role that wavetrains can play in mixing the near-surface heat
705 accumulated in the warm diurnal layer when winds are weak as on 24 February (see the abrupt
706 change in temperature at 4 m depth as waves reach M28; similar evening drops in temperature
707 synchronized with wave packet arrivals are observed on 23 and 25 February).

708 APE^w at M28 and $EKE^w + EKE^{bg}$ at RDIW are presented in Fig. 14 over the entire period of
709 deployments. Several wave packets have clear signatures, both instantaneous and on average over
710 a M2 period, particularly during RL1. For example between 24 February 8 PM and 25 February
711 8:30 AM (Fig. 13) the mean energy at the moorings is 20 J m^{-2} with a near exact equipartition
712 between potential and kinetic wave energy. This yields $F^w = 5 \text{ W m}^{-1}$, in line with mid- and

713 inner-shelf values found off southern California (Lucas et al. 2011b) and Oregon (Torgrimson and
 714 Hickey 1979).

715 An interesting point of comparison can be obtained by computing the speed at which the internal
 716 wave energy can fully mix the water column in the offshore vicinity of the upwelling front and
 717 thus lead to its westward migration. During periods where the upwelling front is near M28 on its
 718 inshore side the IGW flux passing at M28 will be progressively dissipated in a region of across-
 719 shore size L_x between M28 and the upwelling front, inshore of which internal waves cannot exist
 720 because there is no stratification to support them. A fraction γ of this dissipation will be available
 721 for mixing. The typical speed c_{front}^w at which the upwelling front can be displaced seaward by
 722 IGW dissipation is

$$c_{front}^w = L_x \times \frac{\gamma F^w}{\int_{L_x} E^{mix}(x) dx}$$

723 where $E^{mix}(x)$ is the potential energy excess resulting from the homogenization of the stratification
 724 present at cross-shore location x in the hours preceding the arrival of a given wave packet. The
 725 integral concerns the L_x wide region between M28 and the upwelling front. Assuming that E^{mix} is
 726 constant over that restricted area yields $c_{front}^w = \gamma F^w / E^{mix}(M28)$, independant of L_x . E^{mix} values
 727 are in the range 300 to 450 J m⁻² and close to 350 J m⁻² on 24 February afternoon. Assuming a
 728 mixing efficiency $\gamma = 0.2$ (Osborn 1980) leads to $c_{front}^w \approx 250$ m/day. This is modest and would
 729 translate into a 10 km offshore displacement over the duration of our field experiments. There are
 730 however several sources of uncertainties in the calculation, *e.g.*, in the mixing efficiency (Walter
 731 et al. 2014). Perhaps most importantly, the internal wave field energy is estimated at M28 where it
 732 has already been strongly attenuated (through interactions with the bottom and also heterogeneities
 733 of the density field). An estimation performed farther offshore would result in larger F^w . On the
 734 other hand, $\frac{1}{L_x} \int_{L_x} E^{mix} dx$ would also be larger so the outcome in terms of displacement speed

735 c_{front}^w is uncertain. During an earlier field experiment in March 2012 where only moored ADCP
736 measurements are available mid-shelf EKE^w , values of up to 30 J m^{-2} over a tidal period are
737 found while E^{mix} is only marginally larger (UPSEN, Estrade et al, in preparation) so c_{front}^w may
738 reach 1 km per day in some occasions.

739 The complications and uncertainties associated with the alongshore dimension should also be
740 kept in mind. The manifestations of mixing observed at the central and southern transects result
741 from a history of mixing along the 3D path of water parcels. These manifestations tend to be dom-
742 inated by the presence of bulges of mixed water located immediately offshore of regions of strong
743 SST gradients. This is particularly evident where upwelled and warm waters of offshore origin are
744 in contact over the shelf (T6, T10 and to a lesser extent T4). The pathway of the modified sub-
745 surface waters making up these bulges cannot be determined precisely. But general considerations
746 on frontal dynamics suggest that this water may remain trapped in the frontal region while drift-
747 ing alongshore and undergoing IGW mixing. Under upwelling favorable conditions slope waters
748 should preferentially be upwelled onto the shelf in the northern SSUC (Crépon et al. 1984; Ndoye
749 et al. 2014) and subsequently drift equatorward (Ndoye et al., manuscript in preparation), hence
750 the weakest bottom salinities over the shelf found for T1 and T5 and the weaker signs of IGW
751 mixing there. With these considerations in mind, the limitations of our eulerian estimate of IGW
752 mixing potential at one particular location of the mid-shelf at 14°N are evident. IGW trains with
753 the largest amplitude ($\sim 70 \text{ m}$) found during UPSEN2/ECOAO were observed on 28 February
754 around CTD 89 (T8) in 90-100 m water depth. The signature of mixing is noticeable on CTD pro-
755 files performed in the area shortly after their sight (not shown). Whether elevated northern IGW
756 activity contributes to the formation of transformed waters present on 2 March in the frontal area
757 near CTD 108-111 (approx. 50 km to the south) cannot be determined but is consistent with ship

758 ADCP measurements showing southward velocities over the shelf with velocities between 15 and
759 30 cm s^{-1} .

760 Longer term observations at different locations over the shelf would be needed to clarify these
761 issues. They would also allow us to explore the possible relationship between amplitude of the
762 wave packets and the spring-neap cycle. Present observations are ambiguous on this matter be-
763 cause the only neap tide period during the field experiment (centered on 7 March, see Fig. 8e)
764 March) coincided approximately with the lowest mid-shelf stratification.

765 **5. Conclusions**

766 The present study is the first analysis of comprehensive physical in situ observations carried
767 out in the SSUC. A number of findings complement and qualify previously known aspects of the
768 SSUC dynamics.

769 The manner in which the upwelling zone and frontal positions are established has previously
770 been seen, in a 2D vertical subinertial framework, as a consequence of the shutdown of surface
771 Ekman transport in shallow waters. Essential to the conceptual model is the assumption that mo-
772 mentum is sufficiently well mixed inshore of the upwelling zone so that wind and bottom friction
773 equilibrate without involving the Coriolis force (Ekman 1905). In this conceptual model wind
774 strength can modulate the position of the front (Estrade et al. 2008) by affecting surface (Lentz
775 1992) and, more indirectly, bottom turbulence intensity. Overall, our continuous observations re-
776 veal that the water column is rarely destratified and momentum is not well mixed even tens of
777 kilometers inshore of the upwelling front. Although the model may retain some validity at other
778 times or on different time scales, other processes may be more important for the upwelling vari-
779 ability over periods of days to weeks and, in particular, where subsurface water is upwelled, which
780 parts of the shelf it enriches, and how the enriched area and its frontal edge may migrate across-

781 shore with time. In the light of our analyses and findings we hypothesize that two key processes
782 (with possible interplay between them) also play a systemic role in the functioning of the southern
783 Senegal shelf upwelling.

784 First, the upwelling tongue and its frontal separation from the offshore waters are subjected to
785 mesoscale disturbances which bring important non 2D effects. In the northern part of the system,
786 a recurrent expression of mesoscale turbulence during UPSEN2/ECOAO was through 50 – 100
787 km anticyclones that remained quasi-stationary for one to a few weeks offshore of the Cape Verde
788 peninsula. These Cape Verde anticyclones (CVAs) develop as meanders of the system formed
789 by the Mauritanian current and shelf upwelling currents that abut onto the Cape Verde peninsula.
790 CVAs have a clear influence on the shelf upwelling structure. They tend to confine the upwelling
791 tongue nearshore in the northern SSUC and promote offshore export of recent upwelled water near
792 14°N. A better understanding of the unstable behavior of the shelf/slope current system would be
793 useful and, in particular: i) the conditions under which they can influence the shallow parts of
794 the shelf (as around 27 February and possibly at the beginning of the second relaxation - RL2
795 - between 9 and 12 March); ii) their preferential evolution sequences and their relation to envi-
796 ronmental conditions, including wind fluctuations. Our observations are broadly consistent with
797 the fact that shelf current reversals associated with wind relaxations contributed to the flushing of
798 CVA1 and CVA2 away from Cape Verde, although these two structures were strongly diminished
799 in strength at the time of flushing.

800 Another possibly important mechanism affecting the distribution of upwelling and the evolution
801 of the frontal zone is mixing by internal tide dissipation over the shelf. To frame the issue, we find
802 it useful to examine a *fast upwelling* limit case that would be exemplified by central California,
803 where w^{up} is classically tens of meters per day (Capet et al. 2004). In such a situation the upwelling
804 process may be adequately pictured as adiabatic upward advection while vertical mixing is ignored

805 because it merely performs the inescapable incorporation of upwelling water into the mixed layer.
806 This incorporation is tightly slaved to the vertical advection itself. Complexity in vertical mixing,
807 resulting from external processes (*e.g.*, internal tide dissipation) or from heterogeneities directly
808 associated with the upwelling dynamics (*e.g.*, nearshore wind drop-off) can only produce minute
809 changes to where and when upwelling water is entrained into the surface mixed layer. External
810 sources of mixing also have little time to act on upwelling water because w^{up} is large.

811 A radically different type of surface layer enrichment regime has been identified over some
812 shelves where patchy episodes of vertical mixing triggered by inertia-gravity wave activity is the
813 key process that incorporates subsurface water into the euphotic layer while unspecified adiabatic
814 processes are in charge of renewing the pool of bottom water awaiting mixing with surface waters
815 (Sharples et al. 2007; Williams et al. 2013; Tweddle et al. 2013) (see also Lucas et al. 2011b in
816 which southern California internal tides are shown to be responsible for the across-shelf replen-
817 ishing flux of nutrients).

818 The SSUC situation uncovered during UPSEN2/ECOAO may represent an intermediate situa-
819 tion where partial decoupling between upwelling-driven vertical advection and mixing leads to
820 incorporation of bottom water into the surface layer through multiple sporadic mixing episodes.
821 In the SSUC we expect the onshore flow to be strongest near the bottom (Lentz and Chapman
822 2004). Fig. 9 is rather consistent with this as are slope Burger numbers computed in Sec. 3 (one
823 should remain cautious though that the assumption of alongshore invariance essential in Lentz
824 and Chapman 2004 may not apply well given the alongshore flow disruption by Cape Verde). A
825 scaling for upward velocities can thus be constructed as $w^{up} \sim u_b \times s$ where s is the bottom slope
826 and u_b a typical near-bottom cross-shore velocity value. Based on mooring observations reported
827 in this study and consistent with observations in other upwelling sectors a reasonable choice is u_b
828 = 5 cm s^{-1} . Water parcels thus need around 10 days to travel from the shelf break to the mid-shelf

829 upwelling zone and, with a shelf slope around 2 ‰, an estimate for w^{up} is 8 m d^{-1} . This provides
830 ample time for mixing episodes to take place, along complex pathways that evolve under the in-
831 fluence of variable winds and mesoscale activity. As a result, upwelling dynamics may be more
832 disrupted by IGWs in the SSUC than in other upwelling sectors (Schafstall et al. 2010; Avicola
833 et al. 2007).

834 An unknown but presumably significant fraction of the energy driving mixing in the SSUC arises
835 from the fission of internal tides into nonlinear internal waves that subsequently break and dissi-
836 pate. The effect on vertical tracer fluxes is not known at present and depends on the distribution
837 of IGW breaking aided by subinertial (Avicola et al. 2007) and possibly near-inertial shear. The
838 latter was also observed during the experiment (Fig. 9). Based on studies for other shelves this
839 effect deserves careful attention. In particular, it would be interesting to know the extent to which
840 IGW breaking contributes to the enrichment of the shelf euphotic layer in nutrients through ver-
841 tical diffusive fluxes. Relaxation periods when stratification recovers, or the establishment of the
842 Cape Verde anticyclone which enhances shelf stratification, are favorable to internal wave activity
843 and are thus presumably conditions in which these fluxes are particularly strong.

844 Thermohaline heterogeneities efficiently contribute to the disruption of IGW propagation. Dur-
845 ing UPSEN2 and the beginning of ECOAO the upwelling front is well marked and impinges on the
846 continental shelf. Preferential dissipation of IGWs in the offshore vicinity of the upwelling front is
847 supported by many vertical tracer profiles. This has potentially important dynamical implications.
848 Additional observations will be needed to further evaluate the significance of IGWs “pounding“ on
849 the upwelling front in its tendency to migrate offshore. The tentative energetic analysis presented
850 in Sec. 4 leads to upwelling front offshore displacements of a few hundred meters per day which is
851 modest (*e.g.*, in regard to displacements associated with mesoscale disturbances) but uncertainties
852 are large. A more qualitative element supporting the dynamical importance of IGW mixing is the

853 sequence of satellite SST images during UPSEN2/ECOAO that show the progressive erosion of
854 Cape Verde mesoscale anticyclones. Concomitant in situ observations reveal intense interior mix-
855 ing undergone by the thermocline waters within the CVAs. Our interpretation is that CVAs bring
856 substantial stratification over the shelf, which in turn allows IGWs to exist and progressively erode
857 that stratification, *i.e.*, contribute to the CVA decay. On the other hand, SST images do not reveal
858 significant submesoscale frontal activity in comparison to other situations, hence lateral diffusive
859 effects should be modest (Capet et al. 2008c).

860 Fig. 15 helps summarize our main findings and results. The southern Senegal upwelling system
861 is situated over a broad continental shelf. So far, study of this system has overwhelmingly relied on
862 satellite images and has been focused on long time scales (seasonal to interannual, *e.g.*, Lathuilière
863 et al. 2008). The presence of Cape Verde and abrupt change of shelf width in its vicinity must
864 conspire to produce quasi-permanent upwelling intensification just south of the cape, as also found
865 in other upwelling regions, *e.g.*, near Capes Blanco and Mendocino in the California system.
866 The in situ observations we present reveal the complexity and variability of the structure and
867 functioning of the upwelling, that is driven by synoptic wind variability, mesoscale effects and
868 possibly mixing due to superinertial wave activity.

869 The manifestations of mesoscale turbulence involve preferential and persistent patterns that con-
870 nect the shelf and open ocean environment and impact the shelf upwelling dynamics. Superinertial
871 wave activity also seems important for the upwelling sector functioning. Our study provides some
872 indications that internal tides and nonlinear internal gravity waves can play a systemic role in
873 the SSUC through water mass transformation and vertical flux of properties. In sustained up-
874 welling conditions where most of the subsurface water feeding the coastal divergence enters the
875 shelf area in the northern SSUC and subsequently flows southward (Ndoye et al., manuscript in
876 preparation) we expect the stratification to be increasingly impacted by IGWs toward the south

877 (*i.e.*, downstream with respect to the dominant shelf circulation), as we generally observe during
878 UPSEN2-ECOAO. However, water residence time scales over the southern Senegal shelf are com-
879 parable to those of synoptic variability. Water property modifications and biogeochemical activity
880 thus take place along complex pathways that integrate the influence of synoptic wind variability,
881 mesoscale and internal tide activity. How much of that complexity needs to be accounted for to
882 properly understand the ecological functioning of the SSUC (*e.g.*, as a nursery for small pelagic
883 fish) and its long-term evolution will be the subject of future research. Most urgently perhaps, the
884 conditions in which very low dissolved oxygen levels develop over the shelf, as during the final
885 part of UPSEN2/ECOAO experiments, need to be clarified.

886 *Acknowledgments.* We are grateful to the captain and crew of R/V Antá for their dedica-
887 tion and professionalism. We acknowledge financial support from IRD through the AWA
888 and LMI ECLAIRS programs, from LEFE-INSU FUSE, and from FP7 PREFACE. S.N.
889 was supported by the Programme doctoral international modélisation des systèmes complexes
890 UPMC/IRD. Much assistance was provided by Unité de Service IMAGO (IRD, Plouzané),
891 including onland support with satellite imagery by D. Dagherne. We thank B. Le Cann
892 and C. Roy for helpful discussions, and two anonymous reviewers for their insightful and
893 constructive comments on the manuscript. Level 2 SST MODIS and ASCAT data were
894 downloaded from NASA <http://oceancolor.gsfc.nasa.gov/>. QuikSCAT data and [ftp://podaac-](ftp://podaac-ftp.jpl.nasa.gov/allData/ascats/preview/L2/)
895 [ftp.jpl.nasa.gov/allData/ascats/preview/L2/](ftp://podaac-ftp.jpl.nasa.gov/allData/ascats/preview/L2/). Wind data from Dakar weather station were down-
896 loaded at www.ogimet.com/metars.phtml.en.

897 **References**

898 Adams, K. A., J. A. Barth, and F. Chan, 2013: Temporal variability of near-bottom dissolved
899 oxygen during upwelling off central oregon. *J. Geophys. Res.*, **118**, 4839–4854.

- 900 Alford, M. H., and R. Pinkel, 2000: Observations of overturning in the thermocline: The context
901 of ocean mixing. *J. Phys. Oceanogr.*, **30**, 805–832.
- 902 Allen, J., P. Newberger, and J. Federiuk, 1995: Upwelling circulation on the Oregon continental
903 shelf. Part I: Response to idealized forcing. *J. Phys. Oceanogr.*, **25**, 1843–1866.
- 904 Aristegui, J., and Coauthors, 2009: Sub-regional ecosystem variability in the canary current up-
905 welling. *Prog. Oceanogr.*, **83**, 33–48.
- 906 Austin, J. A., and J. A. Barth, 2002: Variation in the position of the upwelling front on the Oregon
907 shelf. *J. Geophys. Res.*, **107**.
- 908 Austin, J. A., and S. J. Lentz, 2002: The inner shelf response to wind-driven upwelling and down-
909 welling*. *J. Phys. Oceanogr.*, **32**, 2171–2193.
- 910 Avicola, G., J. N. Moum, A. Perlin, and M. D. Levine, 2007: Enhanced turbulence due to the
911 superposition of internal gravity waves and a coastal upwelling jet. *J. Geophys. Res.*, **112** (C6).
- 912 Barton, E., 1989: The poleward undercurrent on the eastern boundary of the subtropical North
913 Atlantic. *Poleward Flows Along Eastern Ocean Boundaries*, Springer, 82–95.
- 914 Barton, E. D., 1998: Eastern boundary of the north Atlantic: northwest Africa and Iberia. coastal
915 segment (18, e). *The sea*, **11**, 633–657.
- 916 Barton, E. D., A. Huyer, and R. L. Smith, 1977: Temporal variation observed in the hydrographic
917 regime near Cabo Corveiro in the northwest African upwelling region, February to April 1974.
918 *Deep Sea Res.*, **24** (1), 7–23.
- 919 Boccaletti, G., R. Ferrari, and B. Fox-Kemper, 2007: Mixed layer instabilities and restratification.
920 *J. Phys. Oceanogr.*, 2228–2250.

- 921 Bretherton, F. P., R. E. Davis, and C. Fandry, 1976: A technique for objective analysis and design
922 of oceanographic experiments applied to mode-73. *Deep Sea Res.*, **23**, 559–582.
- 923 Capet, X., E. J. Campos, and A. M. Paiva, 2008a: Submesoscale activity over the Argentinian
924 shelf. *Geophys. Res. Lett.*, **35**, L15 605.
- 925 Capet, X., F. Colas, P. Penven, P. Marchesiello, and J. C. McWilliams, 2008b: Eddies in eastern-
926 boundary subtropical upwelling systems. *Ocean Modeling in an Eddy Regime*, M. Hecht,
927 and H. Hasumi, Eds., Geophys. Monog. Ser., Vol. 177, Am. Geophys. Union.
- 928 Capet, X., P. Klein, B. L. Hua, G. Lapeyre, and J. C. McWilliams, 2008c: Surface kinetic energy
929 transfer in surface quasi-geostrophic flows. *J. Fluid Mech.*, **604**, 165–174.
- 930 Capet, X., P. Marchesiello, and J. C. McWilliams, 2004: Upwelling response to coastal wind
931 profiles. *Geophys. Res. Lett.*, **31**, L13 311.
- 932 Capet, X., J. C. McWilliams, M. J. Molemaker, and A. Shchepetkin, 2008d: Mesoscale to sub-
933 mesoscale transition in the California Current System. part i: Flow structure and eddy flux. *J.*
934 *Phys. Oceanogr.*, **38**, 29–43.
- 935 Capet, X., J. C. McWilliams, M. J. Molemaker, and A. Shchepetkin, 2008e: Mesoscale to sub-
936 mesoscale transition in the California Current System. part ii: Frontal processes. *J. Phys.*
937 *Oceanogr.*, **38**, 44–64.
- 938 Citeau, J., L. Finaud, J. Cammas, and H. Demarcq, 1989: Questions relative to ITCZ migrations
939 over the tropical Atlantic Ocean, sea surface temperature and Senegal River runoff. *Met. Atmos.*
940 *Phys.*, **41**, 181–190.
- 941 Crépon, M., C. Richez, and M. Chartier, 1984: Effects of coastline geometry on upwellings. *J.*
942 *Phys. Oceanogr.*, **14**, 1365–1382.

- 943 Csanady, G. T., 1982: *Circulation in the coastal ocean*. Dordrecht, Holland, 279 pp.
- 944 Demarcq, H., and V. Faure, 2000: Coastal upwelling and associated retention indices derived from
945 satellite sst. application to octopus vulgaris recruitment. *Oceanolo. Acta*, **23**, 391 – 408.
- 946 Dillon, T., 1982: Vertical overturns: A comparison of thorpe and ozmidov length scales. *Journal*
947 *of Geophysical Research: Oceans*, **87 (C12)**, 9601–9613.
- 948 Ekman, V. W., 1905: On the influence of the earth\'s rotation on ocean currents. *Ark. Mat. Astron.*
949 *Fys.*, **2**, 1–53.
- 950 Estrade, P., P. Marchesiello, A. Colin de Verdière, and C. Roy, 2008: Cross-shelf structure of
951 coastal upwelling: A two-dimensional extension of Ekman\'s theory and a mechanism for inner
952 shelf upwelling shut down. *J. Mar. Res.*, **66 (5)**, 589–616.
- 953 Evans, W., B. Hales, P. G. Strutton, R. K. Shearman, and J. A. Barth, 2015: Failure to bloom:
954 Intense upwelling results in negligible phytoplankton response and prolonged co2 outgassing
955 over the oregon shelf. *J. Geophys. Res.*, **120**, 1446–1461.
- 956 Flament, P., L. Armi, and L. Washburn, 1985: The evolving structure of an upwelling filament. *J.*
957 *Geophys. Res.*, **90**, 11 765–11 778.
- 958 Fox-Kemper, B., R. Ferrari, and R. Hallberg, 2008: Parameterization of mixed layer eddies. I:
959 Theory and diagnosis. *J. Phys. Oceanogr.*, **38**, 1145–1165.
- 960 Gan, J., and J. S. Allen, 2002: A modeling study of shelf circulation off northern california in the
961 region of the coastal ocean dynamics experiment 2. simulations and comparisons with observa-
962 tions. *J. Geophys. Res.*, **107**.
- 963 Gan, J., A. Cheung, X. Guo, and L. Li, 2009: Intensified upwelling over a widened shelf in the
964 northeastern south china sea. *J. Geophys. Res.*, **114**.

- 965 Gerkema, T., 1996: A unified model for the generation and fission of internal tides in a rotating
966 ocean. *J. Mar. Res.*, **54**, 421–450.
- 967 Holliday, D., and M. E. McIntyre, 1981: On potential energy density in an incompressible, strati-
968 fied fluid. *J. Fluid Mech.*, **107**, 221–225.
- 969 Hughes, P., and E. Barton, 1974: Stratification and water mass structure in the upwelling area off
970 northwest africa in april/may 1969. *Deep Sea Res.*, **21**, 611–628.
- 971 Huyer, A., J. H. Fleischbein, J. Keister, P. M. Kosro, N. Perlin, R. L. Smith, and P. A. Wheeler,
972 2005: Two coastal upwelling domains in the northern california current system. *J. Mar. Res.*,
973 **63**, 901–929.
- 974 Jackson, C., and J. R. Apel, 2009: An atlas of internal solitary-like waves and their properties,
975 second edition. URL http://www.internalwaveatlas.com/Atlas_index.html.
- 976 Jeans, D., and T. Sherwin, 2001: The evolution and energetics of large amplitude nonlinear internal
977 waves on the portuguese shelf. *J. Mar. Res.*, **59**, 327–353.
- 978 Kang, D., and O. Fringer, 2010: On the calculation of available potential energy in internal wave
979 fields. *J. Phys. Oceanogr.*, **40** (11), 2539–2545.
- 980 Kudela, R. M., and Coauthors, 2008: New insights into the controls and mechanisms of plankton
981 productivity along the US West Coast. *Oceanography*, **21**, 46–59.
- 982 Lamb, K. G., 2014: Internal wave breaking and dissipation mechanisms on the continental
983 slope/shelf. *Annu. Rev. Fluid Mech.*, **46**, 231–254.
- 984 Lathuilière, C., V. Echevin, and M. Lévy, 2008: Seasonal and intraseasonal surface chlorophyll-a
985 variability along the northwest african coast. *J. Geophys. Res.*, **113**.

- 986 Lentz, S. J., 1992: The surface boundary layer in coastal upwelling regions. *J. Phys. Oceanogr.*,
987 **22**, 1517–1539.
- 988 Lentz, S. J., and D. C. Chapman, 2004: The importance of nonlinear cross-shelf momentum flux
989 during wind-driven coastal upwelling. *J. Phys. Oceanogr.*, **34**, 2444–2457.
- 990 Li, Q., and D. M. Farmer, 2011: The generation and evolution of nonlinear internal waves in the
991 deep basin of the south china sea. *J. Phys. Oceanogr.*, **41**, 1345–1363.
- 992 Lucas, A. J., C. L. Dupont, V. Tai, J. L. Largier, B. Palenik, and P. J. Franks, 2011a: The green
993 ribbon: multiscale physical control of phytoplankton productivity and community structure over
994 a narrow continental shelf. *Limnol. Oceanogr.*, **56**, 611–626.
- 995 Lucas, A. J., P. J. Franks, and C. L. Dupont, 2011b: Horizontal internal-tide fluxes support elevated
996 phytoplankton productivity over the inner continental shelf. *Limnol. Oceanogr. Fluids Environ.*,
997 **1 (1)**, 56–74.
- 998 Lucas, A. J., G. C. Pitcher, T. A. Probyn, and R. M. Kudela, 2014: The influence of diurnal winds
999 on phytoplankton dynamics in a coastal upwelling system off southwestern africa. *Deep Sea*
1000 *Res.*, **101**, 50–62.
- 1001 Marchesiello, P., and P. Estrade, 2009: Eddy activity and mixing in upwelling systems: a compar-
1002 ative study of northwest Africa and California regions. *Int. J. Earth Sci.*, **98**, 299–308.
- 1003 Marchesiello, P., J. C. McWilliams, and A. Shchepetkin, 2003: Equilibrium structure and dynam-
1004 ics of the California Current System. *J. Phys. Oceanogr.*, **33**, 753–783.
- 1005 Messié, M., and F. P. Chavez, 2015: Seasonal regulation of primary production in eastern boundary
1006 upwelling systems. *Prog. Oceanogr.*, **134**, 1–18.

- 1007 Millot, C., and M. Crépon, 1981: Inertial oscillations on the continental shelf of the gulf of lions-
1008 observations and theory. *J. Phys. Oceanogr.*, **11**, 639–657.
- 1009 Morison, J., R. Andersen, N. Larson, E. D’Asaro, and T. Boyd, 1994: The correction for thermal-
1010 lag effects in Sea-Bird CTD data. *J. Atm. Ocean Tech.*, **11**, 1151–1164.
- 1011 Moum, J., D. Farmer, E. Shroyer, W. Smyth, and L. Armi, 2007: Dissipative losses in nonlinear
1012 internal waves propagating across the continental shelf. *J. Phys. Oceanogr.*, **37**, 1989–1995.
- 1013 Moum, J., D. Farmer, W. Smyth, L. Armi, and S. Vagle, 2003: Structure and generation of turbu-
1014 lence at interfaces strained by internal solitary waves propagating shoreward over the continental
1015 shelf. *J. Phys. Oceanogr.*, **33**, 2093–2112.
- 1016 Ndoye, S., 2016: Fonctionnement dynamique du centre dupwelling sud-sénégalais: approche par
1017 la modélisation réaliste et lanalyse dobservations satellite de température de la mer. Ph.D. thesis,
1018 Université Pierre et Marie Curie.
- 1019 Ndoye, S., X. Capet, P. Estrade, B. Sow, D. Dagherne, A. Lazar, A. Gaye, and P. Brehmer, 2014:
1020 SST patterns and dynamics of the southern Senegal-Gambia upwelling center. *J. Geophys. Res.*,
1021 **119**, 8315–8335.
- 1022 Osborn, T., 1980: Estimates of the local rate of vertical diffusion from dissipation measurements.
1023 *J. Phys. Oceanogr.*, **10**, 83–89.
- 1024 Pallàs-Sanz, E., T. Johnston, and D. Rudnick, 2010: Frontal dynamics in a california current
1025 system shallow front: 1. frontal processes and tracer structure. *J. Geophys. Res.*, **115**.
- 1026 Palmer, M., G. Stephenson, M. Inall, C. Balfour, A. Düsterhus, and J. Green, 2015: Turbulence
1027 and mixing by internal waves in the celtic sea determined from ocean glider microstructure
1028 measurements. *J. Mar. Sys.*, **144**, 57–69.

- 1029 Pawlowicz, R., B. Beardsley, and S. Lentz, 2002: Classical tidal harmonic analysis including error
1030 estimates in MATLAB using T_TIDE. *Computers & Geosciences*, **28**, 929–937.
- 1031 Peña-Izquierdo, J., J. L. Pelegrí, M. V. Pastor, P. Castellanos, M. Emelianov, M. Gasser, J. Sal-
1032 vador, and E. Vázquez-Domínguez, 2012: The continental slope current system between Cape
1033 Verde and the Canary Islands. *Scien. Mar.*, **76**, 65–78.
- 1034 Pitcher, G., F. Figueiras, B. Hickey, and M. Moita, 2010: The physical oceanography of upwelling
1035 systems and the development of harmful algal blooms. *Prog. Oceanog.*, **85** (1), 5–32.
- 1036 Pringle, J. M., 2002: Enhancement of wind-driven upwelling and downwelling by alongshore
1037 bathymetric variability*. *J. Phys. Oceanogr.*, **32**, 3101–3112.
- 1038 Pringle, J. M., and E. P. Dever, 2009: Dynamics of wind-driven upwelling and relaxation between
1039 monterey bay and point arena: Local-, regional-, and gyre-scale controls. *J. Geophys. Res.*, **114**.
- 1040 Roulet, G., and P. Klein, 2009: Available potential energy diagnosis in a direct numerical simula-
1041 tion of rotating stratified turbulence. *J. Fluid Mech.*, **624**, 45–55.
- 1042 Roy, C., 1998: An upwelling-induced retention area off Senegal: a mechanism to link upwelling
1043 and retention processes. *South Afr. J. Mar. Sci.*, **19**, 89–98.
- 1044 Ryan, J., and Coauthors, 2010: Recurrent frontal slicks of a coastal ocean upwelling shadow. *J.*
1045 *Geophys. Res.*, **115**.
- 1046 Saha, S., and Coauthors, 2010: The ncep climate forecast system reanalysis. *Bull. Am. Meteorol.*
1047 *Soc.*, **91**, 1015–1057.
- 1048 Schafstall, J., M. Dengler, P. Brandt, and H. Bange, 2010: Tidal-induced mixing and diapycnal
1049 nutrient fluxes in the mauritanian upwelling region. *J. Geophys. Res.*, **115**.

- 1050 Sharples, J., and Coauthors, 2007: Spring-neap modulation of internal tide mixing and vertical
1051 nitrate fluxes at a shelf edge in summer. *Limnol. Oceanogr.*, **52**, 1735–1747.
- 1052 Spall, M., 1997: Baroclinic jets in confluent flows. *J. Phys. Oceanogr.*, **27**, 1054–1071.
- 1053 Strub, P. T., P. M. Kosro, and A. Huyer, 1991: The nature of the cold filaments in the California
1054 current system. *J. Geophys. Res.*, **96**, 14 743–14 768.
- 1055 Thompson, A. F., S. T. Gille, J. A. MacKinnon, and J. Sprintall, 2007: Spatial and temporal
1056 patterns of small-scale mixing in Drake passage. *J. Phys. Oceanogr.*, **37** (3), 572–592.
- 1057 Torgrimson, G. M., and B. M. Hickey, 1979: Barotropic and baroclinic tides over the continental
1058 slope and shelf off Oregon. *J. Phys. Oceanogr.*, **9**, 945–961.
- 1059 Tweddle, J. F., J. Sharples, M. R. Palmer, K. Davidson, and S. McNeill, 2013: Enhanced nu-
1060 trient fluxes at the shelf sea seasonal thermocline caused by stratified flow over a bank. *Prog.*
1061 *Oceanog.*, **117**, 37–47.
- 1062 Walter, R. K., M. E. Squibb, C. B. Woodson, J. R. Koseff, and S. G. Monismith, 2014: Stratified
1063 turbulence in the nearshore coastal ocean: Dynamics and evolution in the presence of internal
1064 bores. *J. Geophys. Res.*, **119**, 8709–8730.
- 1065 Wang, D.-P., and A. Jordi, 2011: Surface frontogenesis and thermohaline intrusion in a shelfbreak
1066 front. *Ocean Model.*, **38**, 161–170.
- 1067 Williams, C., J. Sharples, C. Mahaffey, and T. Rippeth, 2013: Wind-driven nutrient pulses to the
1068 subsurface chlorophyll maximum in seasonally stratified shelf seas. *Geophys. Res. Lett.*, **40**,
1069 5467–5472.

- 1070 Woodruff, S., H. Diaz, J. Elms, and S. Worley, 1998: Coads release 2 data and metadata enhance-
1071 ments for improvements of marine surface flux fields. *Physics and Chemistry of the Earth*, **23**,
1072 517–526.
- 1073 Woodson, C., L. Washburn, J. A. Barth, D. Hoover, A. R. Kirincich, M. McManus, J. P. Ryan, and
1074 J. Tyburczy, 2009: Northern monterey bay upwelling shadow front: Observations of a coastally
1075 and surface-trapped buoyant plume. *J. Geophys. Res.*, **114**.
- 1076 Woodson, C., and Coauthors, 2007: Local diurnal upwelling driven by sea breezes in northern
1077 Monterey Bay. *Cont. Shelf Res.*, **27**, 2289–2302.
- 1078 Yu, L., and R. A. Weller, 2007: Objectively analyzed air-sea heat fluxes for the global ice-free
1079 oceans (1981-2005). *Bull. Am. Meteorol. Soc.*, **88**, 527–539.

1080

LIST OF FIGURES

1081 **Fig. 1.** Averaged OSTIA composite SST over the northeastern tropical Atlantic for the pe-
 1082 riod 21 February - 18 March 2013 corresponding to the UPSEN2-ECOAO field ex-
 1083 periments. The image was produced by averaging daily fields downloaded from
 1084 ftp://data.nodc.noaa.gov/pub/data.nodc/ghrsst/L4/GLOB/UKMO/OSTIA. Superimposed is
 1085 a schematic representation of the main circulation features of the region including the North
 1086 Equatorial counter-current (NECC) and the Cape Verde Frontal zone (CVF, thick gray). Our
 1087 study area, the southern Senegal upwelling center (SSUC, black box), stands out as the
 1088 southern tip of the coastal upwelling system. White zonal lines indicate the location of our
 1089 three main hydrological transects. 53

1090 **Fig. 2.** a): Instantaneous (dashed) and low-passed filtered with one inertial period forward shift
 1091 (black solid) meridional wind at DWS [$m s^{-1}$] (negative is southward). b): MODIS zonal
 1092 minimum of nighttime SST averaged meridionally over the northern SSUC (14° - $14^{\circ}30'N$).
 1093 This time series index is insensitive to cross-shore displacements of the upwelling zone. c):
 1094 Longitude of the SST zonal minimum in the latitude range $14^{\circ}N \pm 10'$. Gray dots are es-
 1095 timated from MODIS cloud-free L2 images. Black diamonds are SST minima present in
 1096 TSG temperature along the $14^{\circ}N$ transect. Secondary minima that are less than $0.1^{\circ} C$ (re-
 1097 spectively $0.3^{\circ} C$) warmer than the coldest SST are also indicated with identical (resp. open)
 1098 diamonds. M28 longitude is indicated with the dashed line. d): 2 hourly averaged meridional
 1099 wind measured by the ship weather station when the ship mean position is within 50 km from
 1100 M28. ASCAT measurements within 50 km from M28 (area averaging) are also shown as red
 1101 (resp. blue) crosses for daytime (resp. nighttime) data. e): diurnal wind cycle computed from
 1102 all ship measurements made within 50 km from M28 (arrows with gray lines). Morning and
 1103 evening ASCAT winds for the same period and domain are also represented (black arrows
 1104 at 10:40AM and 10:40PM). In a)-d), abscissa are days from the beginning of the month (Feb.
 1105 or Mar.). Gray rectangles delineate the periods with no shipboard measurements. 54

1106 **Fig. 3.** MODIS SST at different times (given in upper right corner of each image) during the exper-
 1107 iments. CTD transects carried out within 1.5 day (prior or after) of the scene are indicated
 1108 with white dots and labeled on land. Mooring locations are indicated with red square mark-
 1109 ers when they are deployed at the time of the scene. 30 m and 100 m isobath are drawn as
 1110 white lines. Small areas possibly contaminated by clouds are not flagged, *e.g.*, along the line
 1111 that joins ($-18^{\circ}W, 13^{\circ}30'N$ and Cape Verde in panel b). Black dots in panel f) represent the
 1112 position of the $20^{\circ} C$ contour on 8 March 11PM, *i.e.*, about two days before the scene. 55

1113 **Fig. 4.** MODIS SST (top) and ship ADCP velocities (across-shore u , along-shore v) around 27
 1114 February, during an episode of intense onshore flow. The number of individual transects
 1115 contributing to every binned velocity data is also indicated (bottom). 56

1116 **Fig. 5.** Bottom temperature (a), salinity (b), dissolved oxygen (c, in $\mu mol kg^{-1}$, log scale) and fluo-
 1117 rescence (d, log scale) for all CTD casts along the northern (+), central (circles) and southern
 1118 (x) transects carried out during UPSEN2 and ECOAO. Differences between near-surface (s
 1119 subscript) and bottom (b subscript) density are also shown (e), as well as the relationship
 1120 between the temperature and salinity contribution to these differences (f). Isolated dissolved
 1121 oxygen values around or below 1.6 correspond to hypoxic conditions encountered at CTD
 1122 82 and on 16 March during 2 individual CTD casts at $14^{\circ}N$ that are not part of the transect
 1123 series. In panel f, the dashed line indicates where temperature and salinity contributions are
 1124 exactly opposite and compensate each other. 57

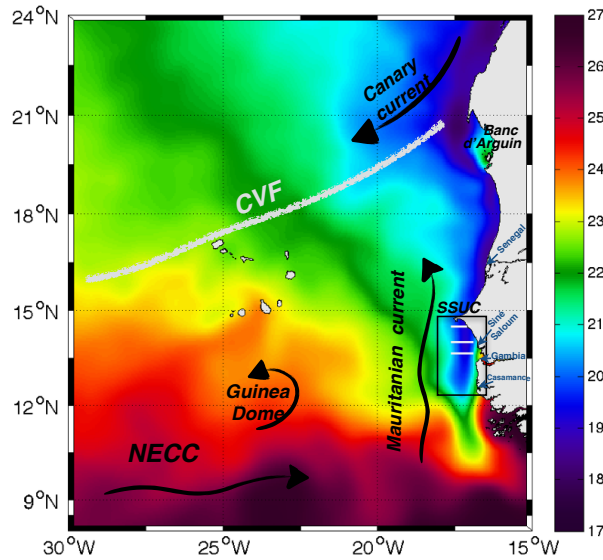
1125 **Fig. 6.** Temperature (left) and salinity (right) CTD transects. See Fig. 7 for details. 58

1126	Fig. 7.	Temperature (left) and salinity (right) CTD transects. Exact longitude range and maximum depth vary. CTD numbers are indicated in gray above the corresponding cast location (dashed line). Transect number, corresponding latitude and time period are indicated in each temperature panel.	59
1127			
1128			
1129			
1130	Fig. 8.	Mid-shelf (M28) time series of temperature at 5 m (a), temperature at 28 m (b), depth integrated heat content (c ; relative to the average over the entire deployment period see text for details), near-surface (5 m) to bottom temperature difference (d), bottom pressure anomaly at RDIE (e, panel range from -1 to +1 dbar) and time-depth temperature diagram (f). The time range shown in a) extends beyond the deployment period to represent MODIS SST before and after the experiment (blue/red symbols for nighttime/daytime scenes). The dashed lines in c) represent heat content trends for a 1D ocean receiving a constant heat flux of 100 or 200 W m ⁻² . The frame delineated with black lines in f) represent the time interval used to compute the typical energy and mixing potential of internal gravity waves in the mid-shelf (Sec. 4).	60
1131			
1132			
1133			
1134			
1135			
1136			
1137			
1138			
1139			
1140	Fig. 9.	Mid-shelf (RDIE) time-depth diagram of detided zonal (<i>i.e.</i> , cross-shore <i>u</i> ; top) and meridional (<i>i.e.</i> , alongshore; bottom) subinertial currents [cm s ⁻¹] over the entire deployment period. The white solid line represent the 0 isocontour. Note the different colorscales for <i>u</i> and <i>v</i>	61
1141			
1142			
1143			
1144	Fig. 10.	Across-shore TSG temperature for 5 transects carried out on 9 March 2013 over time intervals that are specified above each panel, along with the exact latitude of the transect (14°00'N or 14°05'N). Note the rapid changes in temperature distribution with time and latitude.	62
1145			
1146			
1147			
1148	Fig. 11.	Top: 70 kHz echograms obtained on 23 February between 2.22 and 6.00 AM while R/V ANTEA steamed eastward at a nearly constant speed ~ 5 kt. Moderate backscatter levels in blue indicate the position of sharp density gradients. They exhibit oscillations with wavelengths of the order of a few hundred meters embedded into longer internal tides (2 wavelength around 10 km are visible with troughs at 17.47°W, 17.37°W and 17.29°W, and crests at 17.45°W and 17.34°W). Bottom: zoom over the time subinterval 2:58 AM to 3:43 AM indicated by a rectangle in the top panel. Bottom depth measured by the ship ADCP is indicated by a thick black line. Data treatment is performed using the ECHOPEN software (https://svn.mpl.ird.fr/echopen/Echopen_V1.7/).	63
1149			
1150			
1151			
1152			
1153			
1154			
1155			
1156			
1157	Fig. 12.	a): 70 kHz raw echograms obtained on 25 February between 5:00 and 5:40 AM while R/V ANTEA was in station around 14°N, 17°20'W. The position of the CTD is superimposed as white segments forming a zig-zag pattern. b-d): Profiles of temperature (b, with a 1.5° shift between them), anomaly between the measured and stable reordered temperature profile (c, 0.15° C shift), Thorpe displacement (d, [m]; the extremities of the segments below each profile indicate ± 5 m), energy dissipation (e, [W kg ⁻¹] in log scale) and turbulent diffusivity (f, m ² s ⁻¹ in log scale). In e) (resp. f) values below 10 ⁻⁸ (resp. 5 × 10 ⁻⁵) are not shown. Bars corresponding to overturns with temperature amplitudes larger than 0.05° C and N ² > 5 × 10 ⁻⁶ s ⁻² are filled. The latter condition only excludes the minor overturn of cast 8 centered on 30 m depth.	64
1158			
1159			
1160			
1161			
1162			
1163			
1164			
1165			
1166			
1167	Fig. 13.	Time series of: a) vertically integrated eddy kinetic energy and b) vertical velocity at RDIW ; c) 4 m depth temperature, d) vertically integrated available potential energy and e) time-depth temperature diagram at M28. Time period is 24 Feb. 18:20PM to 25 Feb. 2:20AM. <i>i.e.</i> , during the the active period of IGW activity studied in Sec. 4. The depth of the shallowest thermistor is indicated with a black solid line in panel e) (its mean depth over the period	
1168			
1169			
1170			
1171			

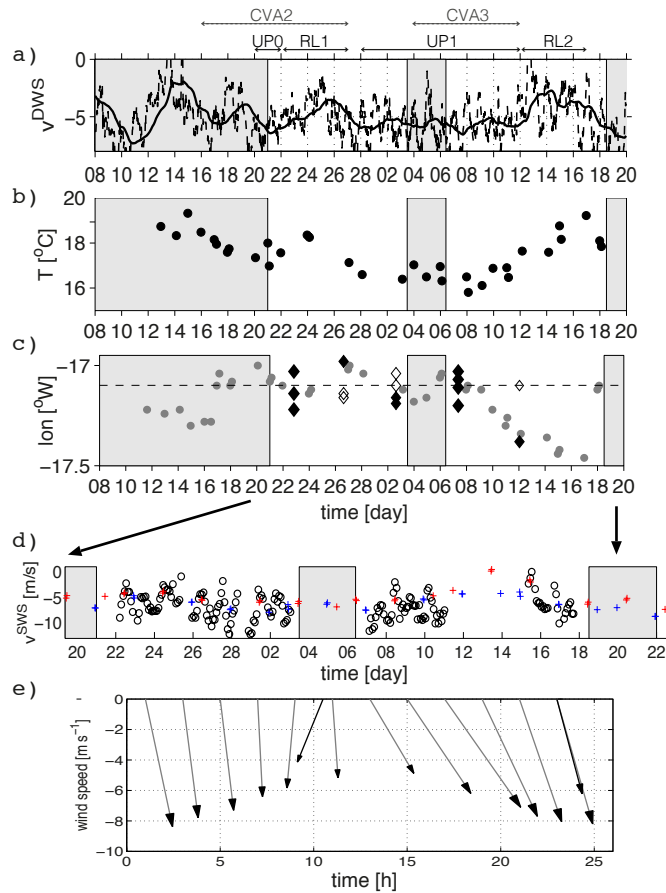
1172 is 3.83 m. Blue arrows in panels a) and d) indicate the times of wave packet arrival used to
1173 estimate c_g (see text for details). The x-axis scale is identical in all panels. 65

1174 **Fig. 14.** Time series of (top) eddy kinetic energy (EKE^w) plus its background level EKE^{bg} (horizontal
1175 white dashed line) and (bottom) available potential energy (APE^w) at M28. In both cases
1176 unfiltered (thin gray) and low-passed (lanczos filter with cut-off at the M2 frequency, black)
1177 signals are shown. Lower signal to noise ratio for EKE^w computed from ADCP observations
1178 is evident. The time interval 24 February 8 PM - 25 February 8:30 AM chosen to estimate
1179 IGW mixing in Sec. 4 is delineated by black dashed vertical lines. 66

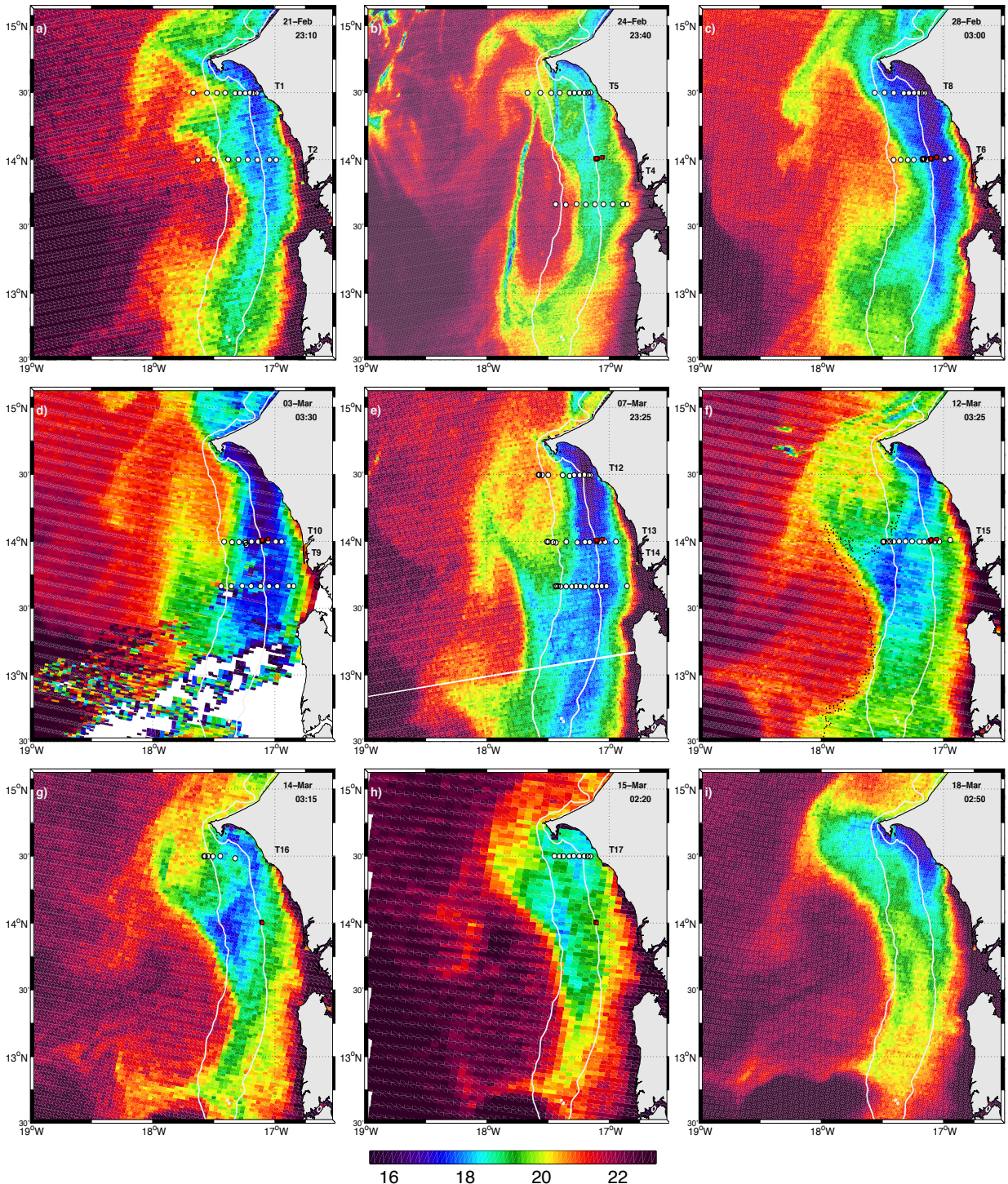
1180 **Fig. 15.** 3D schematic description of the upwelling dynamical and hydrological structure over the
1181 southern Senegal shelf, as observed during UPSEN2-ECOAO. The manifestation of up-
1182 welling takes the form of a cold SST tongue situated tens of kilometers away the shore. Its
1183 position and that of its offshore frontal edge undergo cross-shore displacements influenced
1184 by mesoscale disturbances. These mesoscale disturbances presumably arise from instabil-
1185 ities of the current system composed of the poleward flowing Mauritanian current (MC)
1186 and the equatorward upwelling jet (UJ). One recurrent mesoscale feature is the Cape Verde
1187 anticyclone (CVA) which strongly constrained the flow and hydrological conditions in the
1188 SSUC during the field experiment. Ubiquitous internal gravity waves over the shelf are im-
1189 plicated in water mass transformation (and associated vertical fluxes of properties) that occur
1190 offshore of the upwelling zone. In particular interior mixing is frequently observed just off-
1191 shore of the upwelling zone. Inshore of that zone, the classical 2D Ekman cell (onshore flow
1192 near the bottom, offshore flow in the surface layer) prevails. Therefore, the position of the
1193 upwelling zone may not simply result from the shutdown of the cross-shore Ekman driven
1194 circulation on its inshore flank as in the 2D models of Estrade et al. (2008) and Austin and
1195 Lentz (2002). Partial evidence suggest that IGW breaking may contribute to the offshore
1196 migration of the front during UPSEN2-ECOAO. We hypothesize that the sharpness of the
1197 front separating upwelling and offshore waters is primarily controlled by IGW mixing in the
1198 front area, as opposed to lateral mixing resulting, *e.g.*, from submesoscale frontal dynamics
1199 (which has a limited signature in high-resolution SST images). 67



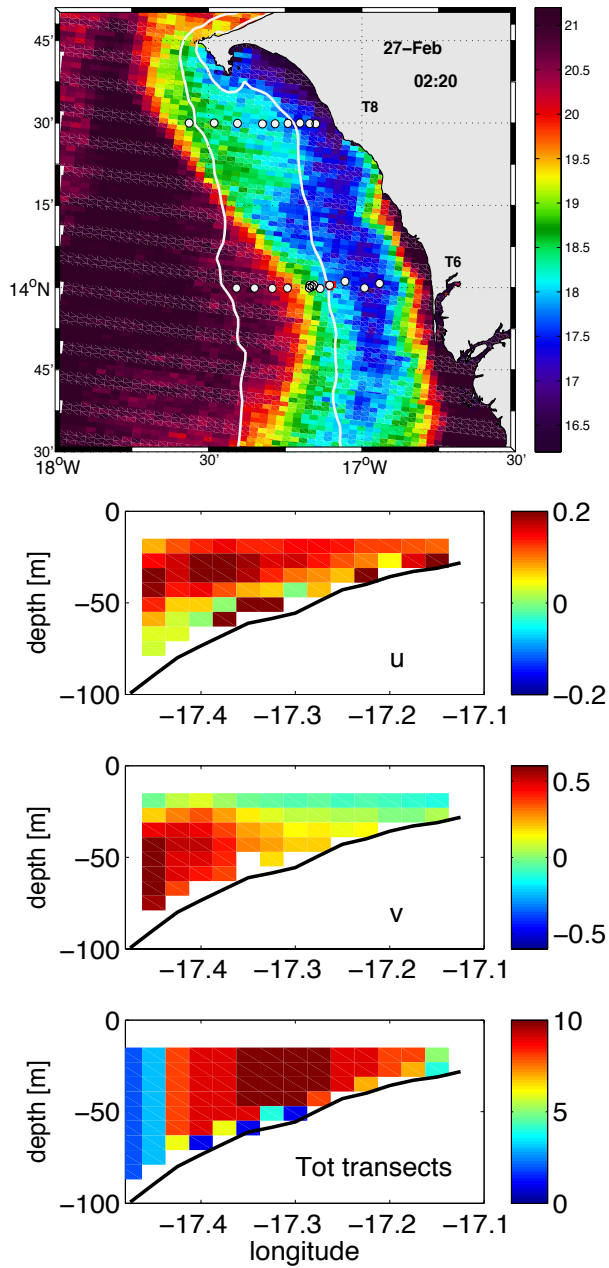
1200 FIG. 1. Averaged OSTIA composite SST over the northeastern tropical Atlantic for the period 21 February
 1201 - 18 March 2013 corresponding to the UPSEN2-ECOAO field experiments. The image was produced by av-
 1202 eraging daily fields downloaded from <ftp://data.nodc.noaa.gov/pub/data.nodc/ghrsst/L4/GLOB/UKMO/OSTIA>.
 1203 Superimposed is a schematic representation of the main circulation features of the region including the North
 1204 Equatorial counter-current (NECC) and the Cape Verde Frontal zone (CVF, thick gray). Our study area, the
 1205 southern Senegal upwelling center (SSUC, black box), stands out as the southern tip of the coastal upwelling
 1206 system. White zonal lines indicate the location of our three main hydrological transects.



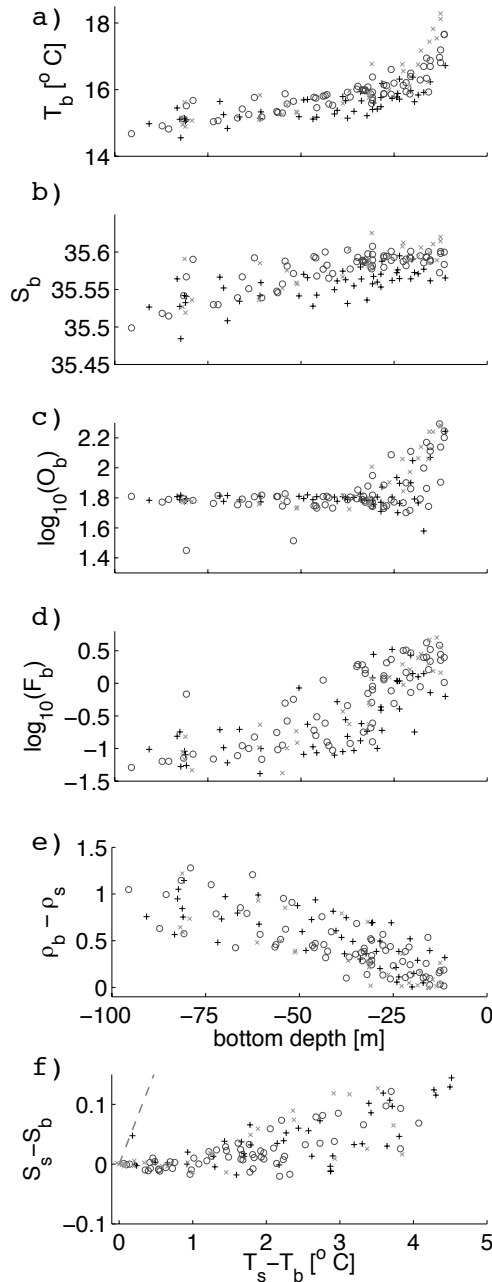
1207 FIG. 2. a): Instantaneous (dashed) and low-passed filtered with one inertial period forward shift (black solid)
 1208 meridional wind at DWS [$m s^{-1}$] (negative is southward). b): MODIS zonal minimum of nighttime SST aver-
 1209 aged meridionally over the northern SSUC (14° - $14^{\circ}30'N$). This time series index is insensitive to cross-shore
 1210 displacements of the upwelling zone. c): Longitude of the SST zonal minimum in the latitude range $14^{\circ}N \pm 10'$.
 1211 Gray dots are estimated from MODIS cloud-free L2 images. Black diamonds are SST minima present in TSG
 1212 temperature along the $14^{\circ}N$ transect. Secondary minima that are less than 0.1° C (respectively 0.3° C)
 1213 warmer than the coldest SST are also indicated with identical (resp. open) diamonds. M28 longitude is indicated with
 1214 the dashed line. d): 2 hourly averaged meridional wind measured by the ship weather station when the ship
 1215 mean position is within 50 km from M28. ASCAT measurements within 50 km from M28 (area averaging) are
 1216 also shown as red (resp. blue) crosses for daytime (resp. nighttime) data. e): diurnal wind cycle computed from
 1217 all ship measurements made within 50 km from M28 (arrows with gray lines). Morning and evening ASCAT
 1218 winds for the same period and domain are also represented (black arrows at 10:40AM and 10:40PM). In a)-d),
 1219 abscissa are days from the beginning of the month (Feb. or Mar.). Gray rectangles delineate the periods with no
 1220 shipboard measurements.



1221 FIG. 3. MODIS SST at different times (given in upper right corner of each image) during the experiments.
 1222 CTD transects carried out within 1.5 day (prior or after) of the scene are indicated with white dots and labeled on
 1223 land. Mooring locations are indicated with red square markers when they are deployed at the time of the scene.
 1224 30 m and 100 m isobath are drawn as white lines. Small areas possibly contaminated by clouds are not flagged,
 1225 *e.g.*, along the line that joins (-18°W,13°30'N and Cape Verde in panel b). Black dots in panel f) represent the
 1226 position of the 20° C contour on 8 March 11PM, *i.e.*, about two days before the scene.



1227 FIG. 4. MODIS SST (top) and ship ADCP velocities (across-shore u , along-shore v) around 27 February,
 1228 during an episode of intense onshore flow. The number of individual transects contributing to every binned
 1229 velocity data is also indicated (bottom).



1230 FIG. 5. Bottom temperature (a), salinity (b), dissolved oxygen (c, in $\mu\text{mol kg}^{-1}$, log scale) and fluorescence (d,
 1231 log scale) for all CTD casts along the northern (+), central (circles) and southern (x) transects carried out during
 1232 UPSEN2 and ECOAO. Differences between near-surface (s subscript) and bottom (b subscript) density are also
 1233 shown (e), as well as the relationship between the temperature and salinity contribution to these differences (f).
 1234 Isolated dissolved oxygen values around or below 1.6 correspond to hypoxic conditions encountered at CTD 82
 1235 and on 16 March during 2 individual CTD casts at 14°N that are not part of the transect series. In panel f, the
 1236 dashed line indicates where temperature and salinity contributions are exactly opposite and compensate each
 1237 other.

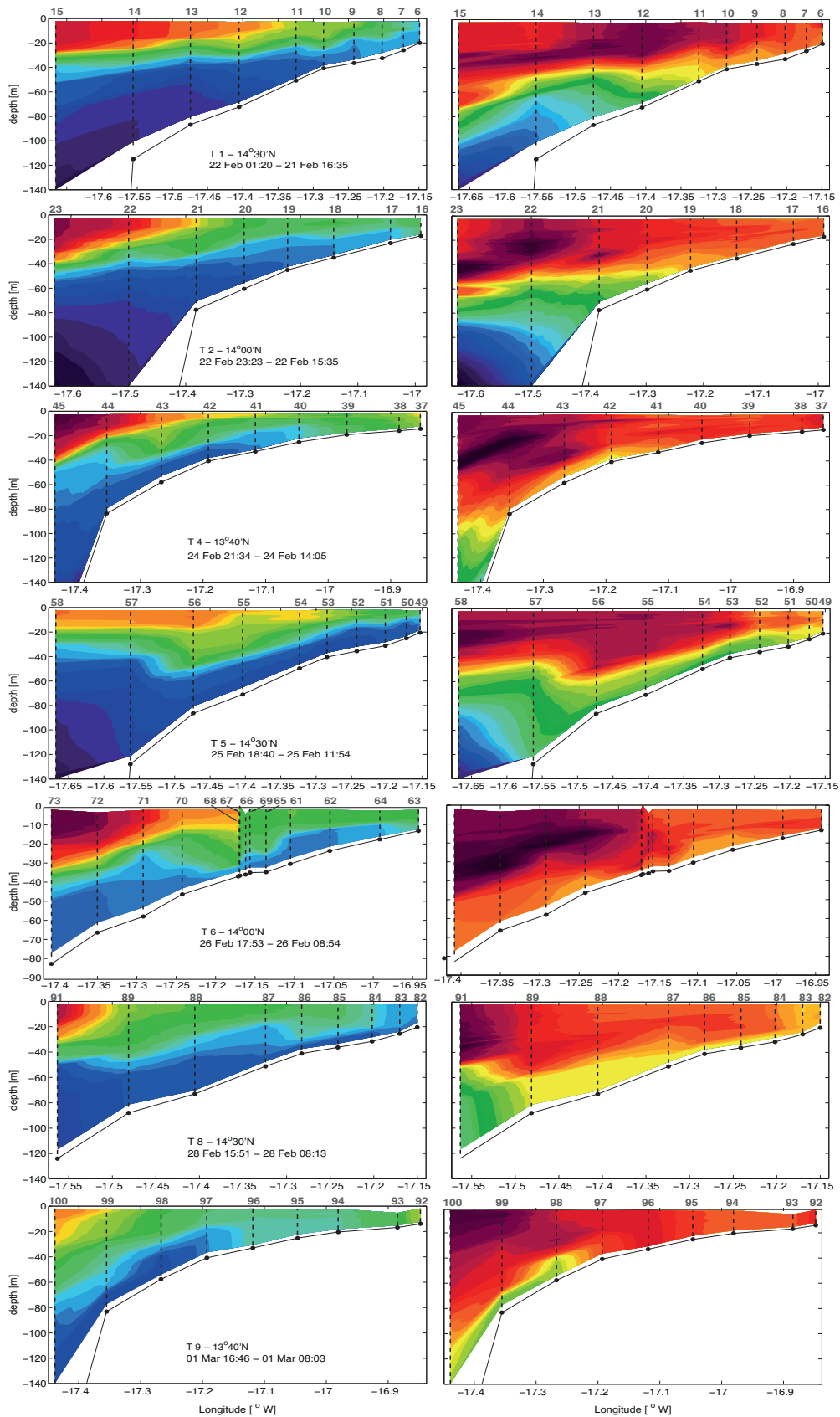
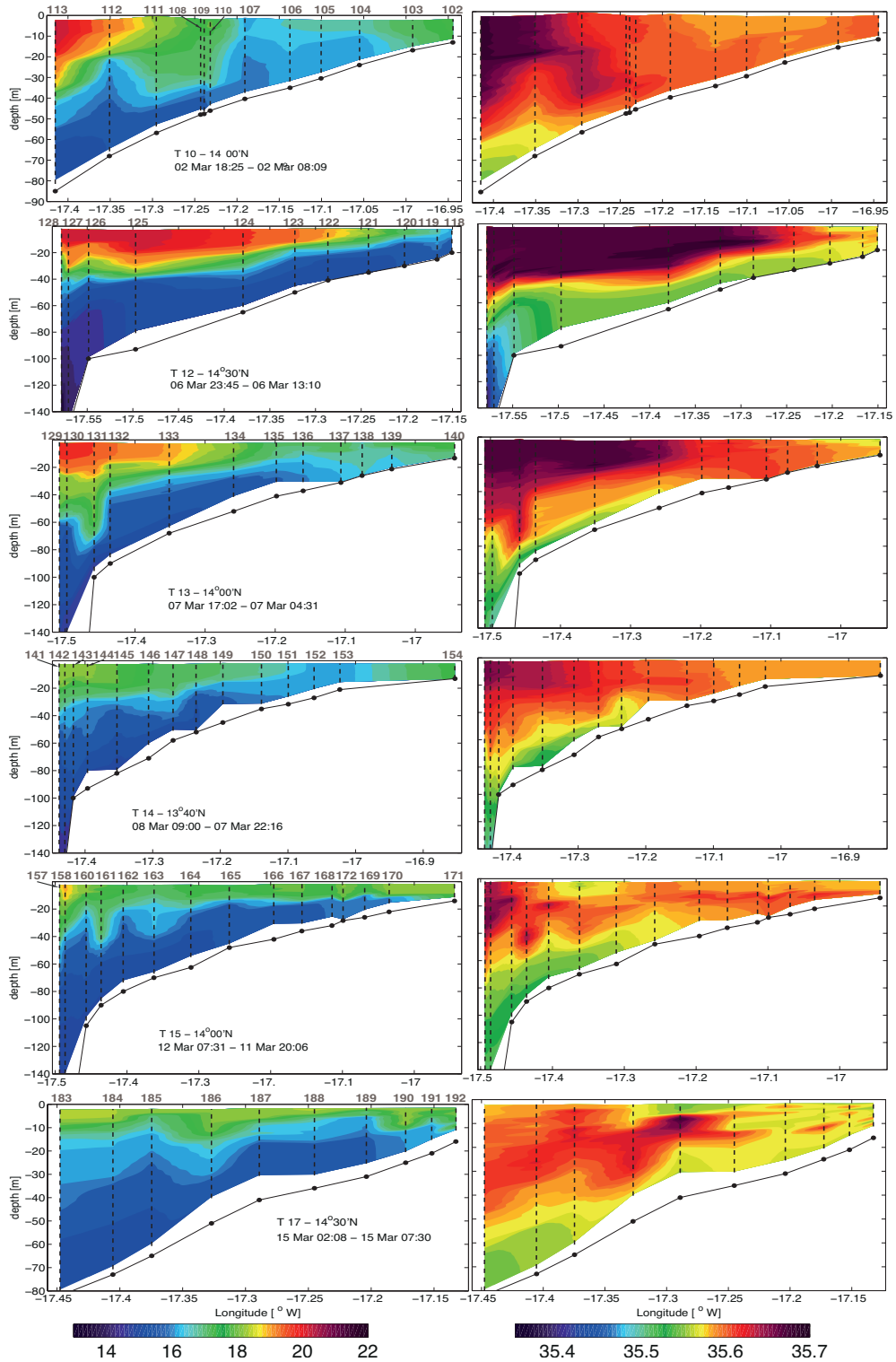
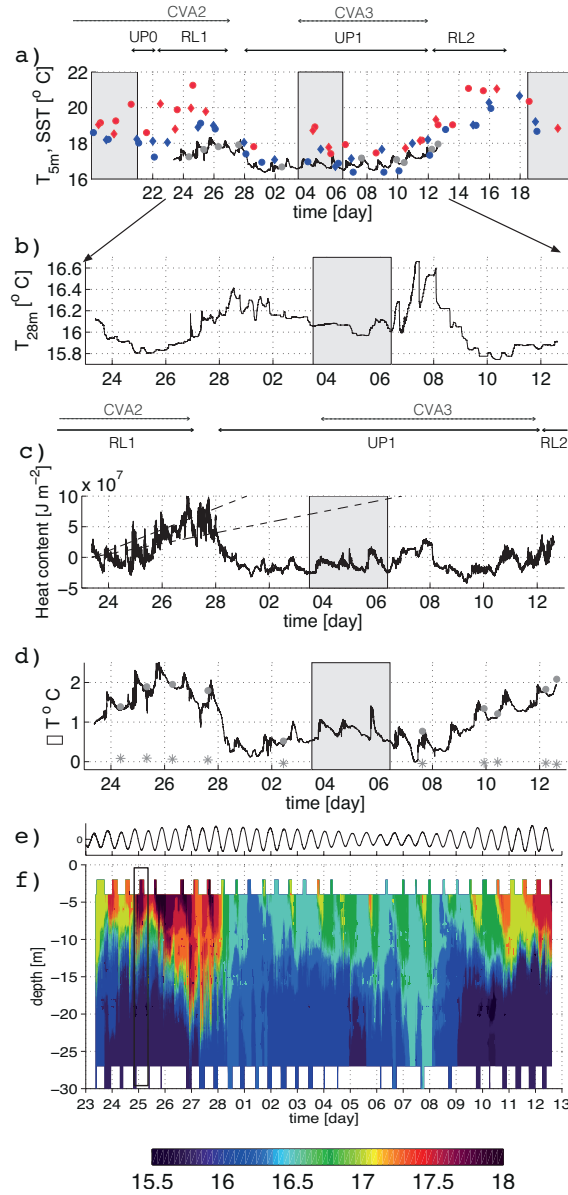


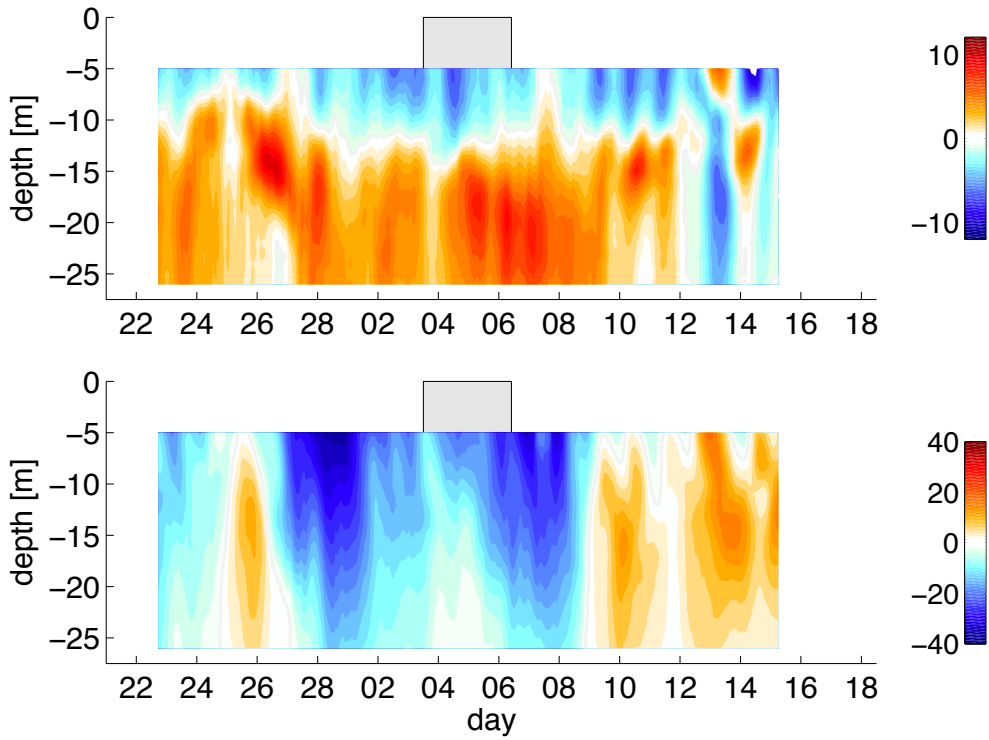
FIG. 6. Temperature (left) and salinity (right) CTD transects. See Fig. 7 for details.



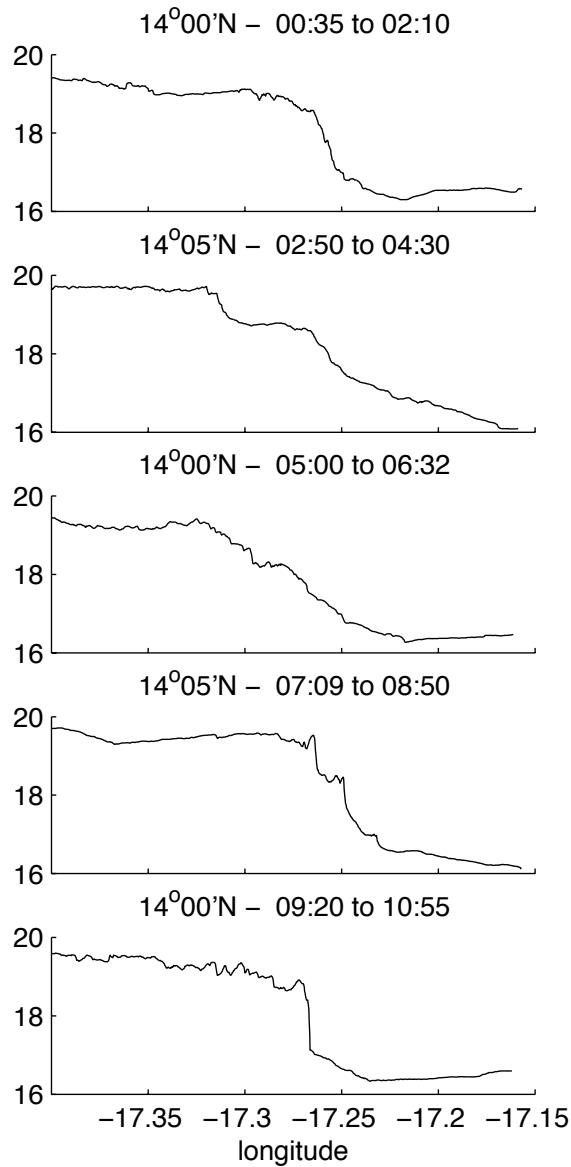
1238 FIG. 7. Temperature (left) and salinity (right) CTD transects. Exact longitude range and maximum depth
 1239 vary. CTD numbers are indicated in gray above the corresponding cast location (dashed line). Transect number,
 1240 corresponding latitude and time period are indicated in each temperature panel.



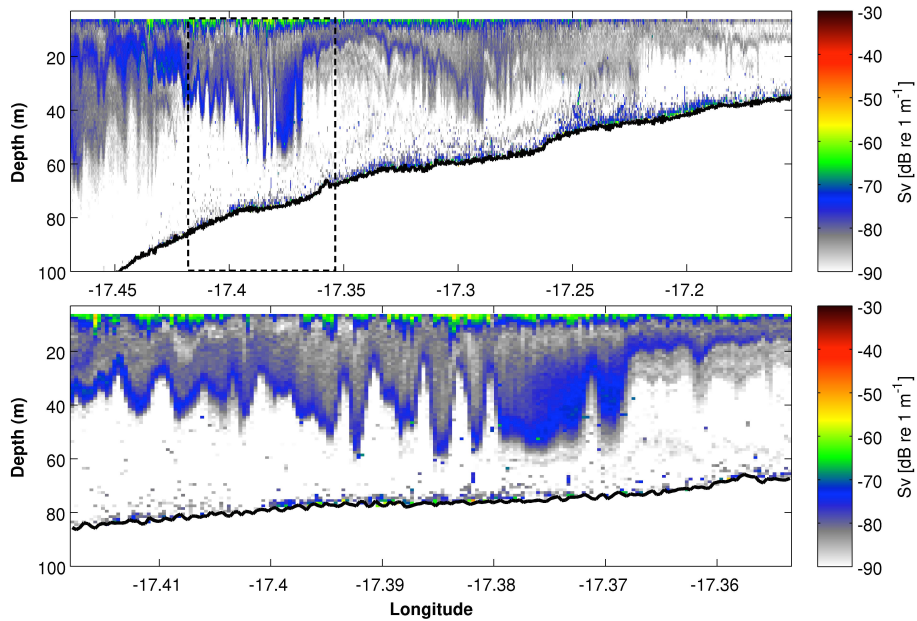
1241 FIG. 8. Mid-shelf (M28) time series of temperature at 5 m (a), temperature at 28 m (b), depth integrated
 1242 heat content (c ; relative to the average over the entire deployment period see text for details), near-surface (5
 1243 m) to bottom temperature difference (d), bottom pressure anomaly at RDIE (e, panel range from -1 to +1 dbar)
 1244 and time-depth temperature diagram (f). The time range shown in a) extends beyond the deployment period to
 1245 represent MODIS SST before and after the experiment (blue/red symbols for nighttime/daytime scenes). The
 1246 dashed lines in c) represent heat content trends for a 1D ocean receiving a constant heat flux of 100 or 200 W
 1247 m⁻². The frame delineated with black lines in f) represent the time interval used to compute the typical energy
 1248 and mixing potential of internal gravity waves in the mid-shelf (Sec. 4).



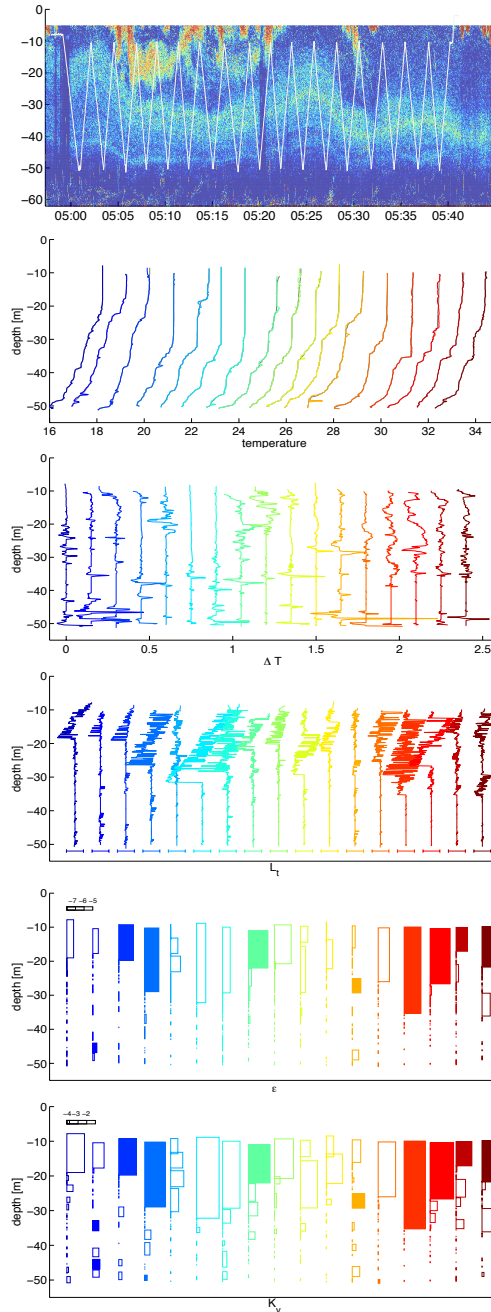
1249 FIG. 9. Mid-shelf (RDIE) time-depth diagram of detided zonal (*i.e.*, cross-shore u ; top) and meridional
 1250 (*i.e.*, alongshore; bottom) subinertial currents [cm s^{-1}] over the entire deployment period. The white solid line
 1251 represent the 0 isocontour. Note the different colorscales for u and v .



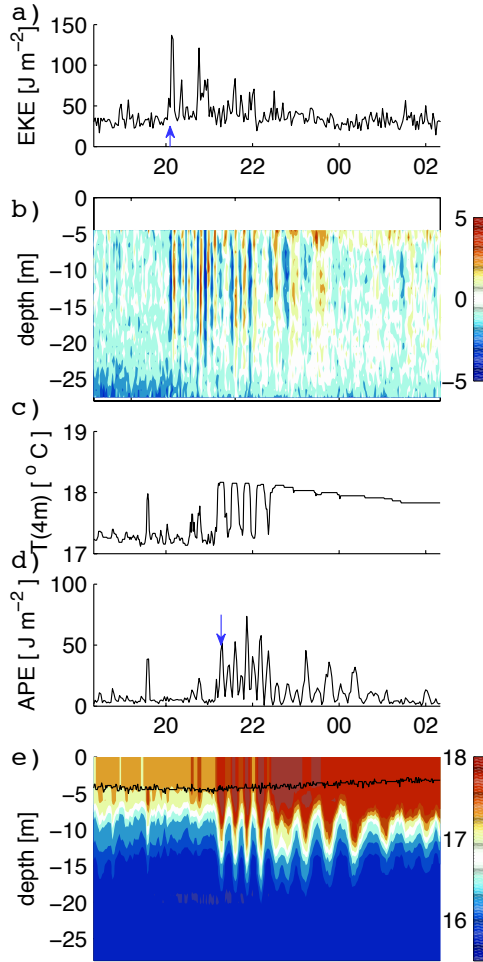
1252 FIG. 10. Across-shore TSG temperature for 5 transects carried out on 9 March 2013 over time intervals that
 1253 are specified above each panel, along with the exact latitude of the transect ($14^{\circ}00'N$ or $14^{\circ}05'N$). Note the
 1254 rapid changes in temperature distribution with time and latitude.



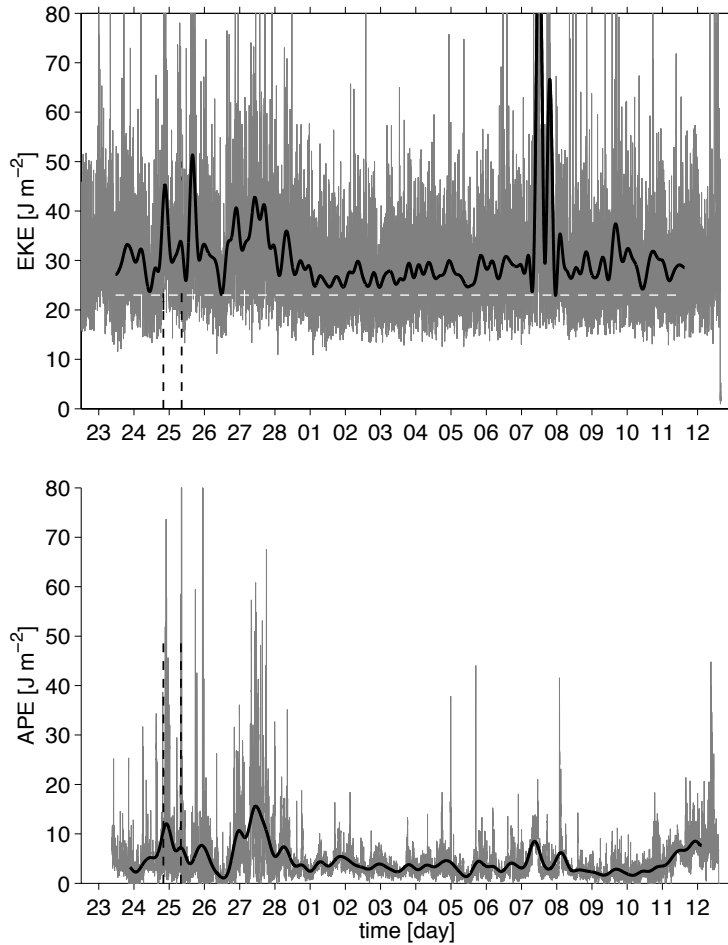
1255 FIG. 11. Top: 70 kHz echograms obtained on 23 February between 2.22 and 6.00 AM while R/V AN-
 1256 TEA steamed eastward at a nearly constant speed ~ 5 kt. Moderate backscatter levels in blue indicate the
 1257 position of sharp density gradients. They exhibit oscillations with wavelengths of the order of a few hun-
 1258 dred meters embedded into longer internal tides (2 wavelength around 10 km are visible with troughs at
 1259 17.47°W , 17.37°W and 17.29°W , and crests at 17.45°W and 17.34°W). Bottom: zoom over the time subin-
 1260 terval 2:58 AM to 3:43 AM indicated by a rectangle in the top panel. Bottom depth measured by the
 1261 ship ADCP is indicated by a thick black line. Data treatment is performed using the ECHOPEN software
 1262 (https://svn.mpl.ird.fr/echopen/Echopen_V1.7/).



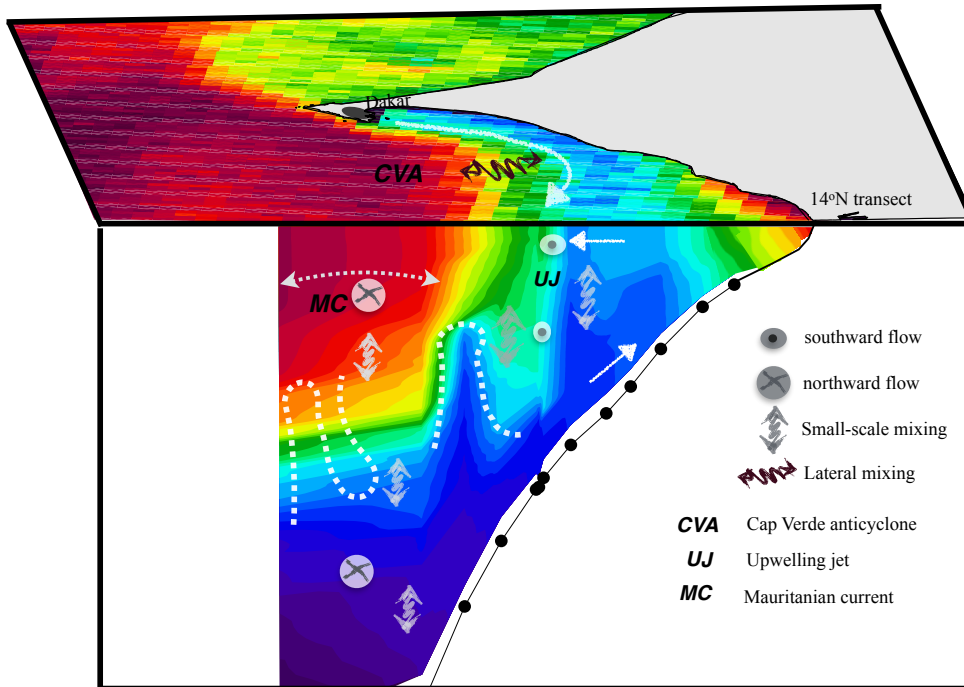
1263 FIG. 12. a): 70 kHz raw echograms obtained on 25 February between 5:00 and 5:40 AM while R/V ANTEA
 1264 was in station around 14°N , $17^{\circ}20'\text{W}$. The position of the CTD is superimposed as white segments forming a zig-
 1265 zag pattern. b-d): Profiles of temperature (b, with a 1.5° shift between them), anomaly between the measured
 1266 and stable reordered temperature profile (c, 0.15° C shift), Thorpe displacement (d, [m]; the extremities of
 1267 the segments below each profile indicate ± 5 m), energy dissipation (e, [W kg^{-1}] in log scale) and turbulent
 1268 diffusivity (f, $\text{m}^2 \text{s}^{-1}$ in log scale). In e) (resp. f) values below 10^{-8} (resp. 5×10^{-5}) are not shown. Bars
 1269 corresponding to overturns with temperature amplitudes larger than 0.05° C and $N^2 > 5 \times 10^{-6} \text{ s}^{-2}$ are filled.
 1270 The latter condition only excludes the minor overturn of cast 8 centered on 30 m depth.



1271 FIG. 13. Time series of: a) vertically integrated eddy kinetic energy and b) vertical velocity at RDIW ; c) 4
 1272 m depth temperature, d) vertically integrated available potential energy and e) time-depth temperature diagram
 1273 at M28. Time period is 24 Feb. 18:20PM to 25 Feb. 2:20AM. *i.e.*, during the the active period of IGW activity
 1274 studied in Sec. 4. The depth of the shallowest thermistor is indicated with a black solid line in panel e) (its mean
 1275 depth over the period is 3.83 m. Blue arrows in panels a) and d) indicate the times of wave packet arrival used
 1276 to estimate c_g (see text for details). The x-axis scale is identical in all panels.



1277 FIG. 14. Time series of (top) eddy kinetic energy (EKE^w) plus its background level EKE^{bg} (horizontal white
 1278 dashed line) and (bottom) available potential energy (APE^w) at M28. In both cases unfiltered (thin gray) and
 1279 low-passed (lanczos filter with cut-off at the M2 frequency, black) signals are shown. Lower signal to noise ratio
 1280 for EKE^w computed from ADCP observations is evident. The time interval 24 February 8 PM - 25 February
 1281 8:30 AM chosen to estimate IGW mixing in Sec. 4 is delineated by black dashed vertical lines.



1282 FIG. 15. 3D schematic description of the upwelling dynamical and hydrological structure over the southern
 1283 Senegal shelf, as observed during UPSEN2-ECOAO. The manifestation of upwelling takes the form of a cold
 1284 SST tongue situated tens of kilometers away the shore. Its position and that of its offshore frontal edge undergo
 1285 cross-shore displacements influenced by mesoscale disturbances. These mesoscale disturbances presumably
 1286 arise from instabilities of the current system composed of the poleward flowing Mauritanian current (MC) and
 1287 the equatorward upwelling jet (UJ). One recurrent mesoscale feature is the Cape Verde anticyclone (CVA) which
 1288 strongly constrained the flow and hydrological conditions in the SSUC during the field experiment. Ubiquitous
 1289 internal gravity waves over the shelf are implicated in water mass transformation (and associated vertical fluxes
 1290 of properties) that occur offshore of the upwelling zone. In particular interior mixing is frequently observed
 1291 just offshore of the upwelling zone. Inshore of that zone, the classical 2D Ekman cell (onshore flow near the
 1292 bottom, offshore flow in the surface layer) prevails. Therefore, the position of the upwelling zone may not
 1293 simply result from the shutdown of the cross-shore Ekman driven circulation on its inshore flank as in the 2D
 1294 models of Estrade et al. (2008) and Austin and Lentz (2002). Partial evidence suggest that IGW breaking may
 1295 contribute to the offshore migration of the front during UPSEN2-ECOAO. We hypothesize that the sharpness of
 1296 the front separating upwelling and offshore waters is primarily controlled by IGW mixing in the front area, as
 1297 opposed to lateral mixing resulting, *e.g.*, from submesoscale frontal dynamics (which has a limited signature in
 1298 high-resolution SST images).